Design and Control of a Musculoskeletal Bionic Leg with Optimized and Sensorized Soft Artificial Muscles

Xuguang Dong, Yixin Wang, Jingyi Zhou, Xin An, Yinglei Zhu, Fugui Xie, Xin-Jun Liu, and Huichan Zhao

***Abstract*—The development of high-performance bionic legged robots can benefit from the continued improvement in design of different actuation methods, including artificial muscles. This work presents a musculoskeletal bionic leg driven by fluidic elastomer actuators (FEAs), demonstrating their potential as artificial muscles for legged robotics. Our approach integrates three key innovations: First, we established a mechanics model based on thin plate theory to optimize the FEAs' bellow shell structure, achieving high force output while maintaining inherent compliance. Second, we developed a lightweight embedded optoelectronic sensing system that enables closed-loop control without adding significant mass. Third, we designed a two-joint bionic leg in the sagittal plane that leverages both monoarticular and biarticular FEA configurations. The leg demonstrated robust performance across various tasks including extreme position movements, load-bearing squats capable of supporting 2.45 times body weight, vertical jumping achieving 147mm ground clearance, and stable walking. Notably, our embedded sensing system successfully detected ground contact states without additional foot sensors, enabling reliable gait control while minimizing complexity and weight. The experimental results validate both the mechanical capabilities of optimized FEAs and their controllability through embedded sensing, establishing a foundation for developing full legged robots with muscle-like actuation.**

***Index Terms*—Biologically-inspired robots, legged robotics, soft sensors and actuators, fluidic elastomer actuator.**

I. Introduction

Legged robotics, particularly quadrupedal robotics, is a rapidly advancing field. With their versatile gaits, terrain adaptability, and maneuverability, quadruped robots have become one of the ideal candidates for search, rescue, and exploration in unstructured environments [1]. Drawing inspiration from the morphology of vertebrates, such as dogs [2], cheetahs [3], horses [4], and turtles[5], there has been significant progress in the functionality and effectiveness of quadruped robots. However, in nature, vertebrate musculoskeletal systems are typically hybrid, combining rigid bones with soft tissues like muscles and tendons [6]. Adapting this configuration for robotics enables precise control and force transmission through the rigid structures, while the soft tissues provide passive environmental adaptation and energy storage. This will allow such legs to be both compliant and capable of executing "natural" motion [7].

Manuscript received xxxx; revised xxxx. This work was supported by the National Natural Science Foundation of China under Grants 52222502, 51975306, and 92048302. (*Corresponding author: Huichan Zhao).*

The authors are with Department of Mechanical Engineering, State Key Laboratory of Tribology in Advanced Equipment, and Beijing Key Lab of Precision/Ultra-Precision Manufacturing Equipment and Control, Tsinghua University, Beijing 100084, China. (e-mail: zhaohuichan@mail.tsinghua.edu.cn)

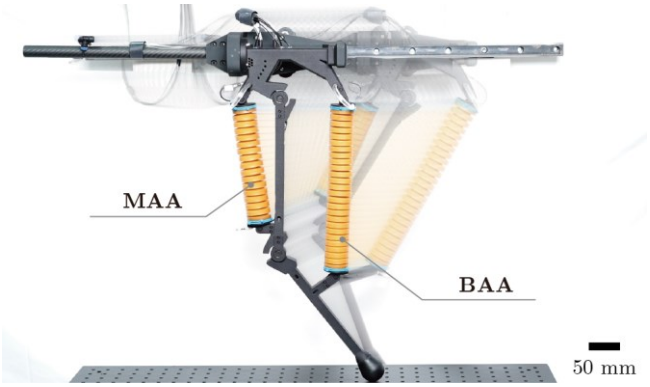

Fig. 1. Snapshots of musculoskeletal bionic leg with two artificial muscles during the single-leg walking. The actuators, which are orange-colored cylindrical components, are integrated into the leg's structure. The monoarticular actuator (MAA) is positioned on the left, while the biarticular actuator (BAA) is on the right.

Artificial muscles are considered promising actuators for musculoskeletal robots [8]. To date, several studies have developed hybrid legged robotic systems based on McKibben muscles, including Ken[9], Pneupard [10], and PneuHound [11] developed by Koh Hosoda's group at Osaka University, Puppy developed by Aschenbeck et al. [12], Cheetah robot developed by Wang et al. [13], and the PIGORASS robot developed by Yamada et al. [14]. Based on the above research, we observe that traditional McKibben muscles offer high output force and energy/power density, but they exhibit relatively low contraction ratios (<25%), significant radial expansion (~100%), and high air consumption. Despite the significant advancements in McKibben-based systems, these factors still present challenges in the development of hybrid robots, affecting the compactness of bioinspired structures and the range of joint motion, as well as increasing the complexity of implementing closed-loop control systems.

With the recent development in the field of soft robotics, the study of s extending, contraction, twisting, etc.) [15, 16]. Despite these advantages, they still face significant challenges for developing future high-performance, bio-comparable hybrid robots, such as (i) how to obtain sufficient force and speed while maintaining their inherent compliance, and (ii) how to achieve proprioception and thus closed-loop control to be as "servo artificial muscles". These challenges are nontrivial due to the inherent nonlinearities and low stiffness of FEA's compositing materials, as well as the high compressibility and the difficulty of controlling air.

For the first problem, legged robots require their muscles to output high forces rapidly to provide sufficient torques for the

leg joints to support the body [3, 17]. Some pioneering work focus on developing high-force FEAs. Zhao et al. [18] adapted rotational casting to fabricate monolithic actuators to avoid delamination during high-pressure application, and Yap et al. [19] employed 3D printing elastic materials with high modulus to enhance the actuators' pressure tolerance and therefore increase the force output. Besides investigating the fabrication methods, novel structural designs such as rigid-soft coupling structures were also demonstrated to effectively enhance pressure tolerance and increase force output. Han et al. [20] and Dong et al. [21] embedded telescopic sleeve into the soft skin of FEAs to constrain their deformation in unexpected directions and amplified forces in the desired directions. Similarly, Zhang et al. [22], Zhu et al. [23], and Cui et al. [24] added external rigid shells to guide the deformation of elastomers into directions in which effective mechanical energy was generated. An alternative way of developing high-force actuator is through the design parameter optimization [25]. In Moseley et al.'s work, finite element analysis was adopted to design FEAs to meet the performance requirement [26]. Liu et al. [27] and Chen et al. [28] utilized the topology optimization method to develop actuators with high forces and other specified performance. We believe the optimization of FEAs is an essential step for maximizing their performance and further integrating into practically functional robots [29].

The second problem is primarily associated with embedding appropriate sensors into the FEAs for closed-loop control. It is necessary for the onboard sensors of legged robots to be lightweight and capable of maintaining high bandwidth as this will minimize the inertia of the legs and ensure that the rapidly changing states can be measured precisely. Currently, researchers are actively conducting studies on embedded sensing methods [30], including but not limited to resistance-based, inductance-based, capacitance-based, and optics-based approaches. Tiziani et al. [31] encapsulated Eutectic Gallium-Indium (EGaIn) within elastomer to create a stretchable resistor, which was then arranged within the chamber of a McKibben actuator to measure its length. Due to the viscoelastic behavior of the elastic materials, resistive sensors usually exhibit hysteresis [32]. Azami et al. [33] developed a linear pneumatic soft actuator in which the inductance of the metal spring varied with its length, and measured the actuator's displacement by measuring the oscillation frequency of a Pierce oscillation circuit. Antonelli et al. [34] integrated a cylindrical capacitor into the telescopic sleeve of an artificial muscle and achieved the length measurement via the capacitance change. Compared with resistive sensors, capacitive and inductive sensors typically exhibit lower hysteresis and better linearity, however, they often require relatively complex instrumentations for measurement. Fiber Bragg grating (FBG) sensors also face similar problems, typically requiring an interrogator. On the other hand, power-modulated optical sensors require only miniature optoelectronics such as infrared Light Emitting Diodes (IR LEDs) and Photoelectric Detectors (PDs) and can measure linear strains with low hysteresis and high repeatability. Zhao et al. [35] integrated stretchable optical waveguides into finger-shape FEAs, giving them the ability to sense bending and force. Tiziani et al. [36], Jun et al. [37], and Jamil et al. [38] all leveraged power-modulated optical sensors to measure the strain of FEAs. Additionally, other existing work have also demonstrated the viability of incorporating angle encoder [39] and microphone [40] into FEAs. These developments all provide the foundation for the development of sensorized and closed-loop controlled artificial muscles.

In this work, we comprehensively study the potential of FEAs as the artificial muscles for quadruped robots. We designed a musculoskeletal bionic leg with two linear FEAs that extended upon positive pressure and contracted upon negative pressure, one as a monoarticular actuator (MAA) and the other as a biarticular actuator (BAA), as shown Fig. 1. To validate the FEAs' mechanical potential, we established a mechanics model for the actuator's bellow shell structure based on thin plate theory, optimized their key parameters to obtain sufficient force, and then characterized their power and energy density in various scenarios. To validate the FEAs' servo controllability, we designed an embedded optical sensing system that did not add extra weight for each actuator and enabled feedback control for the actuators up to 3.6 Hz. Finally, to demonstrate the FEAs' effect in a musculoskeletal configuration, we assembled a bionic leg with two joints in the sagittal plane and performed several important tests critical for legged robots, such as swings to the extreme positions, load-bearing squats, jumping, and path following of its foot. Uniquely, we also leveraged the embedded optical sensors as well as an embedded pressure sensor to estimate the foot's reaction force from the ground, eliminating the need for additional force sensors on the foot-end further reducing leg weight. In the sagittal plane, the leg achieved complete cycles of walking with embedded sensing and feedback control, demonstrating its potential as the basis to form a full quadruped robot.

The paper is organized as follows: Section II provides a description of the structural design, modeling, and parameter optimization of the FEAs and the characterization of the FEAs' mechanical performance. Section III introduces the embedded sensing system and their characterization. Section IV presents the closed-loop control of FEAs with the embedded sensors. Section V presents the design of the bionic leg along with experiment tests and results to demonstrate its performance. Section VI provides a detailed discussion of this work. Finally, in Section VII we summarize the study and present an outlook for possible future work.

II. MODELING AND OPTIMIZATION OF THE FEAS

Our previous work [21] developed a linear bellows-type FEA that incorporates a telescopic sleeve in its air chamber to prevent buckling, thereby enhancing force output. Here, we present an optimized design for hybrid legged robots. Through static modeling and geometric parameter optimization, we have improved the FEA's force output while maintaining operational requirements. Experimental results demonstrate its capabilities in displacement, blocked force, and energy/power density.

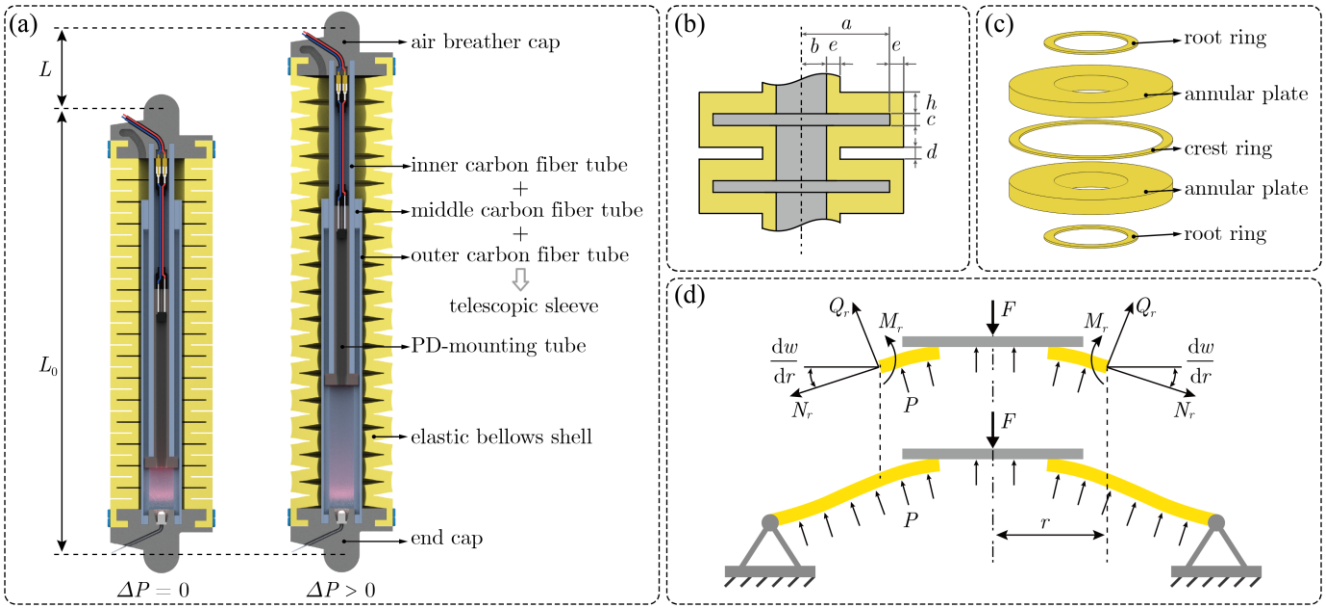

Fig. 2. Structural design and mechanical modeling of FEA. (a) Cross-sectional views of the actuator (MAA) in its initial and pressurized states. (b) Detailed dimensions of the bellows shell segment. Parameters *a* and *b* denote the outer and inner radii of the annular plate, respectively, while *h* represents the plate thickness. Parameters *c*, *d*, and *e* indicate the intra-wave spacing, inter-wave spacing, and wall thickness at crest/root of the bellows, respectively. (c) Components of a single bellows unit. (d) Force analysis of the annular plate under specified assumptions.

A. Actuator structural design

The actuator's architecture is illustrated in Fig. 2a through cross-sectional views of both its initial and freely extended states. The FEA comprises three main components: a bellows-shaped external shell made of elastomeric material, a pair of rigid end caps that anchor the shell, and an internal telescopic sleeve that maintains axial stability by preventing lateral buckling during operation. To achieve robust pneumatic performance, we engineered a mechanical sealing solution by incorporating circumferential grooves into both end caps. These grooves, working in conjunction with zip ties that secure the bellows ends, create an effective sealing interface that maintains chamber airtightness up to 300 kPa while preserving the actuator's full stroke capability.

The sealing mechanism of our proposed FEA differs fundamentally from that of traditional pneumatic cylinders. Conventional cylinders employ a dynamic sealing approach, where rubber or polymer seals maintain contact between the moving piston and the inner cylinder wall. These seals require significant pre-tightening force to maintain airtightness, which generates substantial static friction. For instance, a pneumatic cylinder with a 40 mm inner diameter can exhibit static friction forces up to 50 N. This high friction, particularly pronounced at low speeds, often results in stick-slip motion (crawling). In contrast, our FEA utilizes a static sealing mechanism where the elastic bellows themselves serve as the sealing component. Since no relative motion occurs at the sealing interfaces between the bellows and end caps, the design eliminates the friction-related challenges inherent to traditional cylinders.

The telescopic sleeve mechanism employs three carbon fiber tubes of different diameters, requiring no additional seals between them as they serve purely as guides. The middle tube features longitudinal slots that accommodate an inner sleeve carrying a PD-mounting tube. This design creates two low-friction sliding interfaces: between the carbon fiber tubes themselves, and between the PD-mounting tube and the longitudinal slots in the middle tube. The T-shaped profile of the mounting tube is specifically designed to house a PD which, together with an IR LED, forms an optical waveguide essential for motion sensing and control. Notably, the optical waveguide sensors utilize a non-contact design that eliminates resistance and contact pressure on moving components (detailed in Section III).

By combining static sealing with low-friction telescopic sleeves, our actuator overcomes key limitations of traditional pneumatic cylinders, particularly the high static friction and stick-slip motion that typically impede smooth and precise control of robotic systems. The compliant, lightweight structure enables greater strain capacity while enhancing safety during dynamic interactions and improving biomimetic characteristics.

B. Mechanics modeling

The goal of the model is to establish the relationship between the actuator's geometric dimensions and materials properties, with its force and displacement outputs, which are critical to serve as artificial muscles in bio-inspired robots. We consider the actuator is pressurized at pressure P and with an axial load F. We make the following key assumptions: (1) the telescopic sleeve offers negligible resistance to axial elongation, and (2) torsional and bending moments in the sleeve can be disregarded due to the specific loading conditions. These assumptions are supported by our design configuration, where each actuator end connects to the frame via two bearings that counteract torsional effects and direct external forces to the actuator ends. Thus, we believe these effects do not significantly impact the model's accuracy.

The analysis begins with a single unit of the bellows shell (Fig. 2b), which consists of two root rings, one crest ring, and two annular plates (Fig. 2c). Each crest ring and root ring connected with the outer and inner diameters of the annular plate, respectively. We assume that, during pressurization, deformation primarily occurs in the annular plates, while the crest and root rings maintain their original geometry. The force diagram for each annular plate is shown in Fig. 2d. To analyze the deflection of the axisymmetric annular plate, we use the *von Karman* equations [41] in a polar coordinate system (r, θ). For a material with Young's modulus E and Poisson's ratio μ, the stress φ and deflection w under uniform load q can be expressed as:

$$D\nabla^2\nabla^2 w = \frac{h}{r}\frac{\mathrm{d}}{\mathrm{d}r}\left(\frac{\mathrm{d}\varphi}{\mathrm{d}r}\frac{\mathrm{d}w}{\mathrm{d}r}\right)+q \quad , \tag{0a}$$

$$\nabla^2\nabla^2\varphi = -\frac{E}{r}\frac{\mathrm{d}}{\mathrm{d}r}\left(\frac{1}{2}(\frac{\mathrm{d}w}{\mathrm{d}r})^2\right), \tag{0b}$$

where

$$\nabla^2 = \frac{\mathrm{d}^2}{\mathrm{d}r^2}+\frac{1}{r}\frac{\mathrm{d}}{\mathrm{d}r}=\frac{1}{r}\frac{\mathrm{d}}{\mathrm{d}r}\left(r\frac{\mathrm{d}}{\mathrm{d}r}\right), \tag{1a}$$

$$D=\frac{Eh^3}{12(1-\mu^2)}. \tag{1b}$$

Multiplying both sides of Eq. (0a) and Eq. (0b) by r and integrating with respect to r, the *von Karman* equations can be rewrite as:

$$D\frac{\mathrm{d}}{\mathrm{d}r}\left(\nabla^2 w\right)=\frac{h}{r}\frac{\mathrm{d}\varphi}{\mathrm{d}r}\frac{\mathrm{d}w}{\mathrm{d}r}+\frac{1}{r}\int_0^r qr\mathrm{d}r\,, \tag{2a}$$

$$\frac{\mathrm{d}}{\mathrm{d}r}\left(\nabla^2\varphi\right)=-\frac{E}{2r}(\frac{\mathrm{d}w}{\mathrm{d}r})^2\,. \tag{2b}$$

The radial displacement u, radial boundary force N_r, bending moment M_r, and shear force Q_r can be expressed as functions of deflection w and stress φ using the following equations:

$$u=\frac{r}{E}\left(\frac{\mathrm{d}^2\varphi}{\mathrm{d}r^2}-\frac{\mu}{r}\frac{\mathrm{d}\varphi}{\mathrm{d}r}\right), \tag{4a}$$

$$N_r=h\sigma_r=\frac{h}{r}\frac{\mathrm{d}\varphi}{\mathrm{d}r}, \tag{4b}$$

$$M_r=-D\left(\frac{\mathrm{d}^2 w}{\mathrm{d}r^2}+\frac{\mu}{r}\frac{\mathrm{d}w}{\mathrm{d}r}\right), \tag{4c}$$

$$Q_r=-D\frac{\mathrm{d}}{\mathrm{d}r}\left(\nabla^2 w\right)=-D\frac{\mathrm{d}}{\mathrm{d}r}\left(\frac{1}{r}\frac{\mathrm{d}}{\mathrm{d}r}\left(r\frac{\mathrm{d}w}{\mathrm{d}r}\right)\right). \tag{4d}$$

The governing equations presented above are cited from Ref. [41], which establishes the fundamental differential equations for an axially symmetric loaded flexible circular plate, forming the basis for understanding our actuator's structure. Moreover, with the advancements in numerical methods, these coupled, nonlinear ordinary differential equations (ODEs) can now be solved effectively.

For our specific case, we consider an annular plate under uniform pressure P with its inner edge subjected to axial compressive forces F. The load q in Eq. (2a) is as follows:

$$q=\begin{cases}0, & r<b\\ \dfrac{P\pi(b+e)^2-F}{\pi(b+e)^2-\pi b^2}, & b\le r\le b+e\\ P, & b+e<r\le a\end{cases}. \tag{5}$$

Let's consider the boundary conditions at the inner edge ($r = b$) and outer edge ($r = a$) of the annular plate, ensuring that they satisfy the specified constraints.

(1) At $r = b$, the inner edge cannot rotate freely and can move radially:

$$\frac{\mathrm{d}w}{\mathrm{d}r}=0\,,\ \frac{\mathrm{d}\varphi}{\mathrm{d}r}=0\,. \tag{6}$$

(2) At $r = a$, the outer edge can rotate freely but cannot move radially:

$$M_r=0\,,\ u=0\,. \tag{7}$$

We employed MATLAB's bvp5c solver [42] to solve this boundary value problem (BVP) by substituting boundary conditions. Before applying bvp5c to solve the BVP problem, the second-order ODEs, Eq. (2a) and Eq.(2b), should be transformed into a system of first-order ODEs. The solver produces continuous first-order derivatives dw/dr and dφ/dr across the interval [b, a]. Through integration of these first-order derivatives, we can obtain the distribution of deflection w and stress φ. Let $w_{\max}$ denote the maximum deflection of each annular plate at the inner edge. The total elongation L of the n-wave bellows-shape actuator is given by:

$$L=\sum_{i=1}^{2n} w_{\max}\,. \tag{8}$$

The initial length L_0 and initial cavity volume V_0 of the bellows shell can be expressed as:

$$L_0=n(2h+d)+(n-1)c\,, \tag{9a}$$

$$V_0=\pi b^2 n(2h+d)+\pi a^2(n-1)c\,. \tag{9b}$$

C. Optimization objective

In this part, we will introduce an optimization problem to design actuator parameters that meet specific mechanical properties and achieve high component integration. Our approach begins by determining the actuators' operational constraints through kinematic and static analyses. Specifically, we obtained the required axial stroke range [$L_{\min}$, $L_{\max}$] and radial boundary [$R_{\min}$, $R_{\max}$] from the leg's theoretical workspace via kinematics. The actuators' blocked forces (F_b) are determined from load-bearing requirements via statics analysis (detailed in the section IV-C).

The optimization framework is developed considering a set of predetermined parameters including $L_{\min}$, $L_{\max}$, $R_{\min}$, $R_{\max}$, F_b, E, σ_m, and μ. Discrete design variables, such as n, a, b, c, d, e, and h, are adjusted during the design process to achieve optimal

design outcomes. Our optimization strategy addresses three key objectives:

(1) Minimize the required pressure P_b for generating the blocked force F_b at maximum actuator extension L_{max}, improving operational efficiency.

(2) Minimize the internal volume V_0 of the structure to enhance both energy efficiency and structural compactness.

(3) Maximize the critical buckling force F_{cr} at initial length L_0 to ensure robust structural stability [43].

To address this multi-objective combinatorial optimization problem (MOCOP), we employ the evaluation function method. These objectives are weighted and combined into an objective function U, which is to be minimized:

$$\min\ U = \lambda_1 P_b^{'} + \lambda_2 V_0^{'} + \lambda_3 F_{cr}^{'} . \tag{10}$$

The weighting coefficients λ_1, λ_2 and λ_3 are introduced to balance the relative importance of each objective. We assign values of 0.4, 0.3, and 0.3 to λ_1, λ_2 and λ_3 respectively, with a primary focus on minimizing pressure. To address the dimensional heterogeneity of the objectives, we normalize P_b, V_0 and F_{cr} using MATLAB's MAPMINMAX function. The critical force F_{cr} is normalized to the interval [1,0], while the pressure P_b and volume V_0 are mapped to the interval [0,1]. This normalization ensures that minimizing P_b and V_0 while maximizing F_{cr} aligns with the overall goal of minimizing U.

D. Constraints

The optimization of actuator structures is subject to multiple constraints that ensure practical feasibility. These constraints encompass manufacturing limitations, geometric requirements, and material properties. All physical quantities are expressed in standard units: millimeters (mm) for length, Pascal (Pa) for pressure, and Newton (N) for force.

(1) The design must accommodate a telescopic sleeve, requiring a minimum inner radius R_{min}, while the outer radius is limited to R_{max} due to space constraints:

$$R_{min} \le b < a + e \le R_{max} . \tag{11}$$

(2) The established model relies on the thin plate theory. Therefore, the annular plate should satisfy the dimensional requirement as a thin plate:

$$\frac{h}{2a} \le \frac{1}{5} . \tag{12}$$

(3) To prevent excessive material deformation within the axial stroke range [L_{min}, L_{max}], the theoretical maximum deflection is constrained by kh, where k is set to 3 in this work:

$$w_{max}^{t} = \frac{L_{max} - L_0}{2n} \le kh . \tag{13}$$

(4) During axial compression, the bellows structure reaches a critical state where corrugation gaps completely disappear and the structure no longer exhibits visible gaps. This compressed state leads to a significant increase in the actuator's stiffness, enhancing its load-bearing capacity. At this point, the bellows behaves as an equivalent hollow cylinder, leading to the following equation:

$$nd = (n-1)c . \tag{14}$$

(5) The number of corrugations n is determined by dividing the total length by the length of a single corrugation. It must be a positive integer:

$$n = \frac{L_{min} + L_c}{2h + d} \in N^{+} . \tag{15}$$

In Eq. (15), L_c represents a buffer distance to prevent the telescopic sleeve from severe impact at L_{min}. This buffer allows for 6-8 mm compression in MAA and 9-11 mm in BAA before reaching L_{min}.

(6) We manufacture the elastic bellows shell using a casting method with a specially designed split mold system (Fig. 3a). The external molds, CNC-machined from 6061 aluminum alloy, provide durability and precision. Resin-printed annular plate insets form the corrugation gaps, while other internal components are also 3D printed. The resin molds' heat-softening properties enable easier demolding through hot water treatment when needed. Additionally, considering the stiffness of the annular plate insets, the flowability of pre-elastomer in the assembled mold, and the precision of the 3D printer, we set dimensional limit for the spacings:

$$c \ge 0.5 ,\ d \ge 0.5 ,\ e \ge 0.5 ,\ h \ge 0.5 . \tag{16}$$

(7) Through finite element analysis [21], we know that the maximum stress in the bellows structure occurs at the crest ring. Following the fourth strength theory, the maximum equivalent stress σ_{eq} in the crest ring must not exceed the material's allowable strength σ_{allow}:

$$\sigma_{eq} = \sqrt{3}\frac{(a+e)^2}{(a+e)^2 - a^2} \le \sigma_{allow} , \tag{17a}$$

$$\sigma_{allow} = \sigma_m / \eta . \tag{17b}$$

The equivalent stress is derived from enclosed thick-walled cylinder [44]. In Eq.(17b)., σ_m represents the material's tensile strength and η is the safety factor (set to 3). We selected VytaFlex60 (Smooth-On Inc.) as the elastomeric material for its combination of high mechanical properties (100% modulus E~2 MPa, tensile strength σ_m~6 MPa) and excellent fluidity in its pre-elastomer state.

E. Optimization algorithm

The optimization process consisted of two main steps: feasible solution exploration and optimal parameter selection. In the first step, we implemented an enumeration-based method (see Appendix A: Algorithm 1) to systematically explore the feasible solution space for each actuator. This method evaluated discrete combinations of structural parameters while satisfying all constraints defined in Section II-D. The algorithm generated a comprehensive map of viable solutions, as visualized in the three-dimensional parameter space shown in Fig. 3b.

In the second step, we employed the unity function U defined in Section II-C to identify the optimal design parameters among the feasible solutions. The optimization results for both actuators are visualized as pentagon symbols in their respective solution space plots. By evaluating U across different parameter groups, as shown in the objective function plots, we identified solutions that effectively balance the three competing objectives: minimizing required pressure (P_b),

reducing initial cavity volume (V_0), and maximizing critical buckling force (F_{cr}).

A key design decision was to maintain unified structural parameters between the MAA and BAA, varying only the number of corrugations. This unified design approach significantly simplifies the manufacturing process by allowing the use of the same mold components, as illustrated in Fig. 3a, while still achieving the required functional differentiation through different actuator lengths. The final optimized parameters and their corresponding performance metrics are presented in the results table in Fig. 3b.

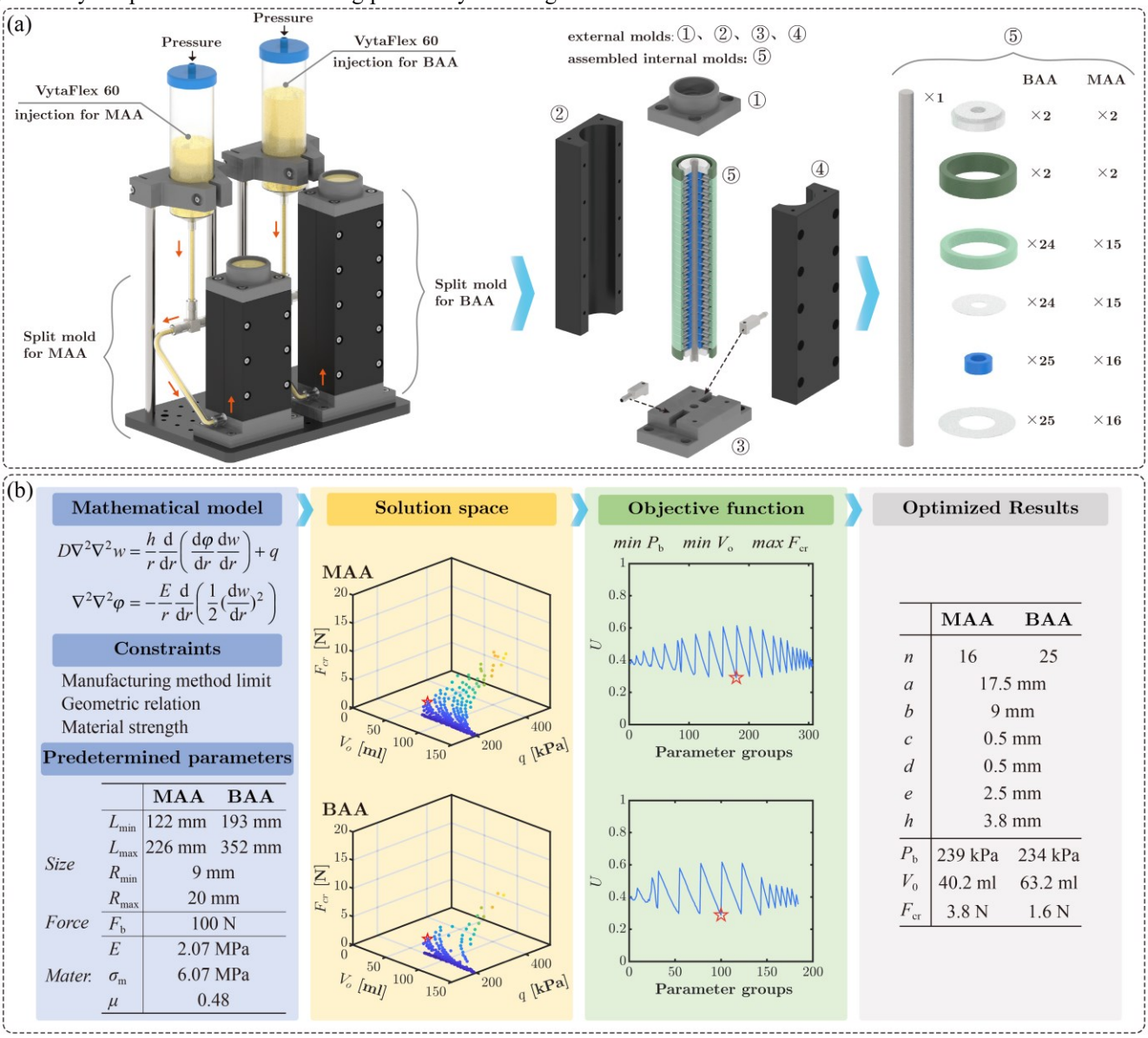

		MAA	BAA
Size	L_{min}	122 mm	193 mm
	L_{max}	226 mm	352 mm
	R_{min}	9 mm	
	R_{max}	20 mm	
Force	F_b	100 N	
Mater.	E	2.07 MPa	
	σ_m	6.07 MPa	
	μ	0.48	

	MAA	BAA
n	16	25
a	17.5 mm	
b	9 mm	
c	0.5 mm	
d	0.5 mm	
e	2.5 mm	
h	3.8 mm	
P_b	239 kPa	234 kPa
V_0	40.2 ml	63.2 ml
F_{cr}	3.8 N	1.6 N

Fig. 3. Manufacturing process and optimization workflow of the FEAs. (a) Split mold system configuration: left part shows the assembly and injection process for MAA and BAA actuators; right part illustrates the exploded view of manufacturing components including external molds (①-④), assembled internal molds (⑤), and the required quantities of each component for both actuators. (b) The overview of the FEAs optimization comprising four parts: mathematical model with governing equations and constraints, solution space visualization for both actuators, objective function evaluation showing the normalized U across parameter groups, and optimized results presenting the final structural parameters and performance metrics.

F. Characterization

Based on the optimized parameters, we fabricated two bellows shells and assembled them as FEAs, weighing 196 g and 294 g for the MAA and BAA, respectively. The characterization setup (Fig. 4a) included a stepper motor with a ball screw mechanism for linear motion control, a magnetostrictive displacement sensor (MDS, THM Series, Shenzhen Milont Technology Co., Ltd.) for position measurement, and the FEA's breather cap mounted on the slider with a magnetic ring and force sensor. The electrical signals (shown in green) represent voltage output for various measurements, while the pneumatic connections (shown in blue) represent air supply for the FEA.

Model predictions and experimental results (Fig. 4b) showed nonlinear behavior in free displacement, with discrepancies primarily arising from simplified thin plate boundary conditions and the use of a linear elastic model for

nonlinear material. However, despite some discrepancies in blocked forces, the model predictions are generally in line with the experimental results. Both blocked forces and strokes meet the predetermined parameters outlined in Fig. 2b, confirming the effectiveness of the proposed model and optimization approach.

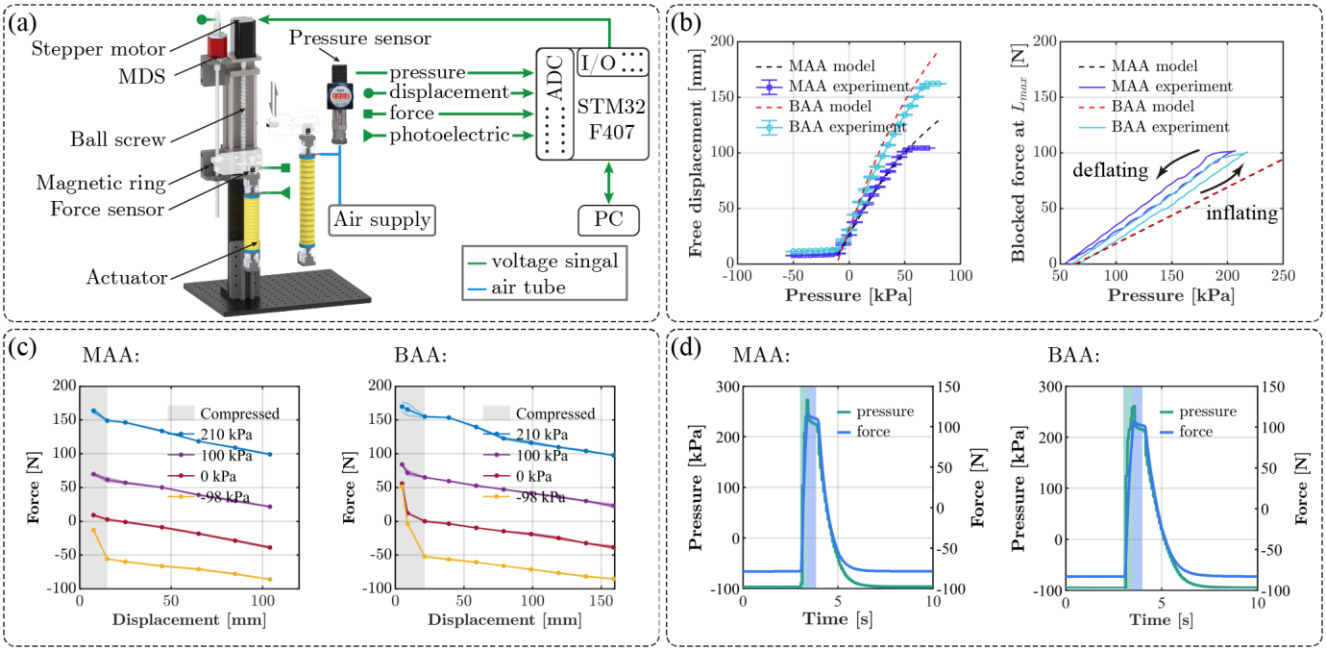

Fig. 4. Characterization of the optimized FEAs. (a) Experimental platform for actuator characterization. (b) The static mechanical properties of MAA and BAA. Left: free displacement versus pressure. Right: blocked force versus pressure. (c) Force-displacement of FEAs at different pressures, where the gray area indicates the compression region. (d) Dynamic response of the blocked force and pressure versus time. Green Area: Inflating valve ON, deflating valve OFF. Blue Area: Both inflating and deflating valves OFF. Other Areas: inflating valve OFF, deflating valve ON.

The force-displacement characteristics of the FEAs (Fig. 4c) demonstrated approximately 100 N of blocked force at maximum stroke. Under positive pressure conditions (210 kPa), this resulted in energy densities of 55.1 kJ·m^{-3} and 64.1 kJ·m^{-3} for MAA and BAA, respectively. Under negative pressure conditions (-98 kPa), the energy densities for MAA and BAA are 31.1 kJ·m^{-3} and 30.7 kJ·m^{-3}, respectively. These energy densities substantially exceed those of natural muscles, which typically range from 8 kJ·m^{-3} and can reach up to 39 kJ·m^{-3} [45]. Furthermore, our FEAs exhibit remarkable strain capabilities, reaching 61% and 65% for MAA and BAA, respectively, compared to their unpressurized resting state. These values far exceed the performance of skeletal muscle (20 - 40%).

The dynamic response characterization of the FEAs under the conditions of 400 kPa inflation and -98 kPa deflation is illustrated in Fig. 4d. The inflation and deflation of the FEA are controlled via two flow control valves (FCVs, YCLT21 series, Yuyao Yongchuang Solenoid Valve Co., Ltd.) each with a 2 mm orifice diameter. During inflation, the power densities of the MAA and BAA are 740 kW·m^{-3} and 780 kW·m^{-3}, respectively. In contrast, during deflation, these values are 66 kW·m^{-3} for MAA and 55 kW·m^{-3} for BAA. These power densities are comparable to those of natural muscles, which typically range from 50 kW·m^{-3}, reaching up to a maximum of 248 kW·m^{-3} [45]. Additionally, both the MAA and BAA achieve impressive strain rates of 570% s^{-1} during extension to the maximum stroke. These rates substantially exceed the typical range of 10-50% s^{-1} for skeletal muscle, highlighting their excellent potential for dynamic applications. However, their contraction rates (50 % s^{-1} and 40 % s^{-1}) reveal an asymmetric performance profile that should be considered when designing mechanisms and control systems involving these actuators.

Having completed the design, optimization, and characterization of the FEAs, we have demonstrated their potential for further development in advanced robotic applications.

III. Sensing and Control of the FEAs

Proprioceptive sensing is fundamental for control of legged robots with artificial muscles. We developed an optical waveguide sensor within the FEA's rigid telescopic sleeve, which forms an enclosed, light-isolated environment, as shown in Fig. 5a. The telescopic structure maintains precise alignment between the light emitter and detector while effectively shielding the sensor from ambient light. By measuring the light intensity at the detector end, we achieve non-invasive length measurement with minimal weight addition.

A. Optoelectronic sensor design

The optoelectronic sensing system used for proposed FEAs is shown in Fig. 5a. An IR LED mounted in the end cap emits infrared light, which undergoes reflection and absorption along the inner wall of the sleeve before being captured by a photodetector positioned within the PD-mounting tube. The light propagates through two interconnected cylindrical channels: channel 1, with a variable length x_1 that changes with actuator displacement, and channel 2, with a fixed length x_2.

The associated circuitry is detailed in Fig. 5b. The PD converts the received light into an electrical signal U_s, with two

key adjustable parameters: R_{LED} controls the emission intensity of the IR LED, while R_{PD} modulates the output signal range of U_s. We defined a baseline light intensity I_0, measured at the PD when x_1 is at its minimum position. The output power loss (PL) in decibels is then calculated relative to this baseline, where I denoting the current light intensity:

$$PL = 10\log_{10}(\frac{I_0}{I}) . \quad (18)$$

Since light intensity is a power quantity, it can be represented by the dissipation power calculated from the voltage U_s. Therefore, the PL in the optical waveguide can be expressed as:

$$PL = 20\log_{10}(\frac{U_v - U_0}{U_v - U_s}) . \quad (19)$$

In Eq.(19), U_0 is the potential difference across the PD when the optical waveguide is at its minimum length, and U_v denotes the circuit supply voltage of 5V.

The encapsulation of the sensing system is shown in Fig. 5c. The PD-mounting tube is integrated into the inner telescopic sleeve, creating an enclosed, light-isolated environment in conjunction with the outer telescopic sleeve and the end cap. Additionally, the PD is installed at the end of the PD-mounting tube, with the PD wiring connected to the air inlet end cap via a detachable connector. This integrated structural design seamlessly embeds the IR LED and PD within the end cap and telescopic sleeve, achieving a fully integrated actuator-sensor assembly.

Geometrical optics simulations in COMSOL enable qualitative analysis of how reflective properties influence sensor performance. These simulations provided valuable insights for material selection and optimization of light source emission angles in sensor design. The geometric model consists of two cylinders (Fig. 5a) with vanishing boundary conditions

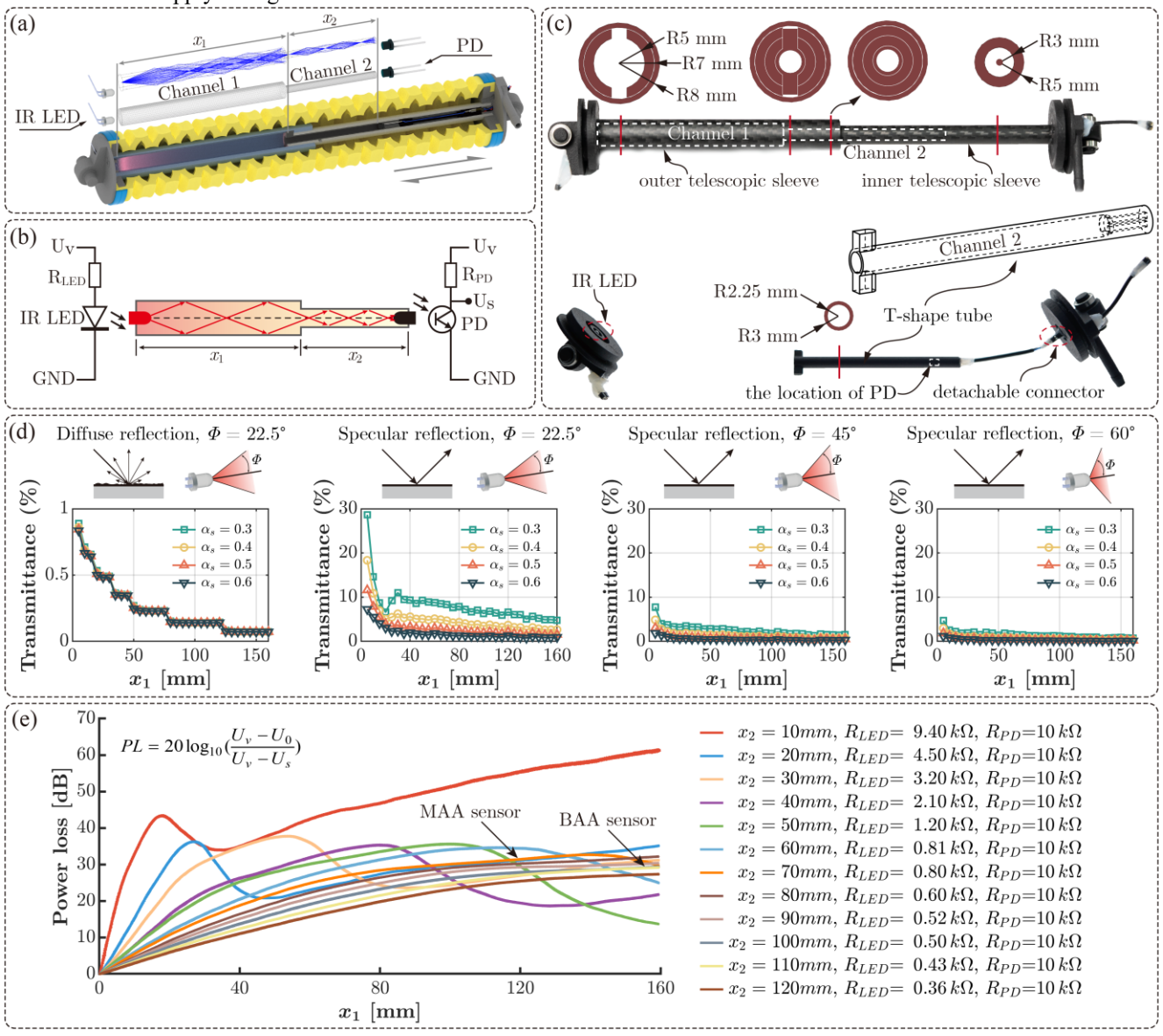

Fig. 5. Displacement sensing system of the FEA. (a) Diagram of the sensing system with simulated light rays (using the MAA as an example). (b) Circuits of the sensing system. (c) Encapsulation of the sensing system. (d) Simulated transmittance as influenced by different reflection conditions. (e) Experimental results of PL versus displacement x_1 for different PD-mounting tube lengths x_2.

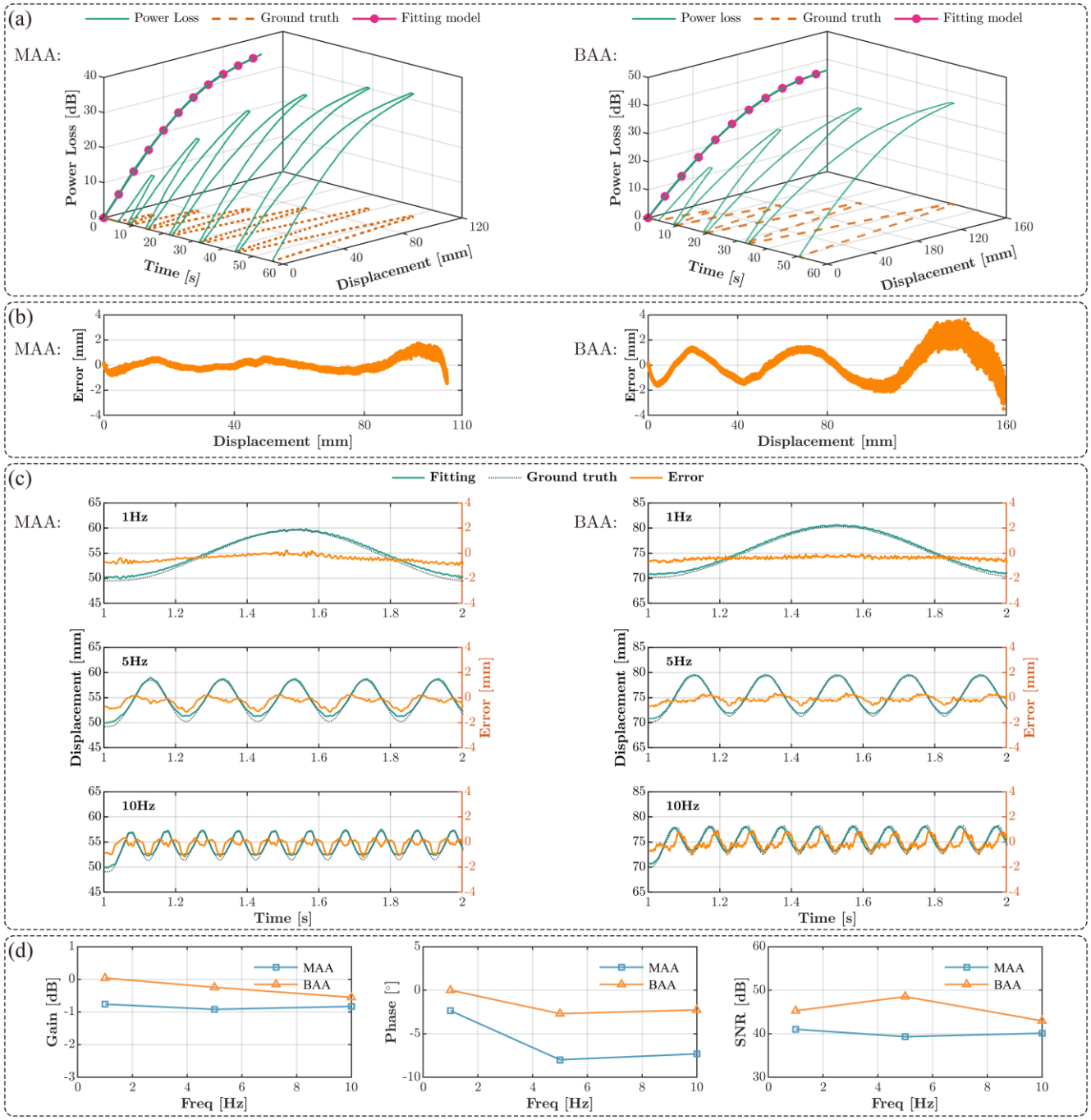

Fig. 6. Sensing system characterization in the FEAs. (a) Temporal relationship between displacement x_1 and *PL* for the MAA (left) and BAA (right). (c) Sensor dynamic response at varying frequencies. (d) Frequency-dependent gain, phase, and SNR characteristics of the MAA and BAA sensors.

at both ends and the junction. The inner walls are subjected to mixed diffuse/specular reflection, with some potential absorption. The absorption coefficient (α_s) represents light loss during reflection, and transmittance, expressed as a percentage, indicates the light intensity received by the PD. We conducted a parametric sweep of x_1, ranging from 5 to 160 mm in 5 mm steps, maintaining x_2 at 60 mm.

The simulation results (Fig. 5d) demonstrate that diffuse reflection reduces transmittance, with minimal effect from different absorption coefficients. Specular reflection, however, exhibits more complex behavior. At low absorption coefficient ($\alpha_s = 0.3$) and small emission angle ($\Phi = 22.5°$), transmittance shows nonlinear and non-monotonic behavior, which weakens as α_s increases. For a fixed α_s, a narrower LED emission angle leads to a wider range of transmittance variation. Therefore, it is crucial to select the appropriate tube material and the LED emission angle to optimize the sensor's response. Based on these results, we selected black nylon material with a high α_s for 3D-printing the PD-mounting tube, and IR LED with a 15° emission angle to improve sensing sensitivity through a wider range of transmittance variation.

We conducted experimental quantitative analysis of the PD-mounting tube length x_2 using the setup illustrated in Fig. 4a. We measured displacement x_1 using MDS and fabricated

PD-mounting tubes via 3D printing with x_2 ranging from 10 to 120 mm. To ensure that the only variable was x_2, we maintained constant IR LED emission angle and R_{PD} while adjusted R_{LED} to maintain U_0 at 1 V. We evaluated sensor response over a displacement range of 0 to 160 mm, and results are shown in Fig. 5e. When x_2 was short (e.g., 10 mm), *PL* showed non-monotonic and nonlinear with respect to x_1. We determined the optimal x_2 length by ensuring monotonic *PL* response with maximum variation within the required stroke range. Consequently, we set x_2 to 60 mm for the MAA and 80 mm for the BAA.

Finally, we modulated the resistances R_{PD} and R_{LED}. In this work, the R_{PD} and R_{LED} for MAA are 3.9 kΩ and 390 Ω, respectively, while for BAA, they are 5.6 kΩ and 300 Ω.

B. Calibration and characterization

After integrating the modulated photoelectric sensor into the FEA, we calibrated the sensor's *PL* response to the displacement x_1. The FEA was subjected to reciprocating stretching at a constant speed of 20 mm/s with varying amplitudes, while both the displacement x_1 from MDS and the output voltage U_s of reception circuit were recorded. As shown in Fig. 6a, MAA underwent six stretching cycles with displacements of 20 mm, 40 mm, 60 mm, 80 mm, 100 mm, and 105 mm, while BAA was subjected to four stretching cycles with displacements of 40 mm, 80 mm, 120 mm, and 160 mm. The resulting 3D visualizations demonstrate *PL* variations across time and displacement domains. The solid lines depict the *PL* response during cyclic stretching at different stroke lengths, while dotted lines represent the corresponding displacement trajectories. Notably, no obvious hysteresis was observed, demonstrating the high repeatability and stability of the sensing system. Furthermore, the embedded optical sensor is low-cost (less than 1 RMB) and lightweight, adding only 2.5g per FEA.

To address the sensor's non-linear behavior, we applied 6th-order polynomial curve fitting. This order was empirically chosen to balance accuracy and avoid overfitting, as lower-order polynomials resulted in substantial errors, while higher-order polynomials provided minimal improvement in accuracy. The model's accuracy was validated against experimental data across the motion range, as shown in Fig. 6a. Further analysis of the results, presented in Fig. 6b, reveals that fitting errors increase in magnitude with FEA extension. The maximum absolute errors for the MAA and BAA are 1.7 mm and 3.7 mm (1.6% and 2.3% full-scale accuracy), while the MAE are 0.4 mm and 0.9 mm (0.4% and 0.6% full-scale accuracy), respectively.

Dynamic performance was evaluated using 10 mm amplitude sinusoidal trajectories at 1 Hz, 5 Hz, and 10 Hz. Fig. 6c compares calibrated sensor output (solid lines) against MDS ground truth (dotted lines), demonstrating close temporal correlation. The sensing errors remained within the millimeter range, increasing slightly with frequency. At 10 Hz, the maximum error was 1.14 mm for MAA (1.1% of the task scope) and 1.32 mm for BAA (0.8% of the task scope).

The frequency-domain characteristics of the sensors were analyzed based on time-domain data, as shown in Fig. 6d. The gain response indicates consistent amplitude response across tested frequencies, with attenuation remaining within -3dB. The phase response shows a minimal offset (greater than -8°), indicating negligible signal lag. These characteristics suggest an effective bandwidth exceeding 10 Hz.

Additionally, we calculated the signal-to-noise ratio (SNR) of the sensors based on the time-domain data. Within our measurement range, the average SNR of MMA and BAA are 40 dB and 45 dB, respectively, demonstrating robust noise immunity and high signal fidelity.

C. Closed-loop control of the FEA

We developed and validated a closed-loop control architecture incorporating real-time displacement feedback from our embedded sensing system. The control system architecture for a single actuator, shown in Fig. 7a, employs two FCVs that modulate air flow through current signals from their respective drivers. The inflating valve connects a 400 kPa pressure source to the actuator, while the deflating valve provides a -80 kPa exhaust pathway. A cascaded PID controller, implemented on an STM32F407 microcontroller running at 1 kHz, generates PWM signals that are transmitted to the FCV's driver. Position feedback from the embedded sensor is digitized through an ADC (AD7606, Analog Devices, Inc.) and fed back to the controller. We empirically tuned the cascaded PID parameters to ensure robust performance across diverse operating conditions.

To evaluate the closed-loop performance, we conducted a series of trajectory tracking experiments using sinusoidal reference inputs of varying frequencies and amplitudes. By analyzing the FEA's dynamic response measured by the MDS, photoelectric sensor, and pressure sensor, we generated Bode plots revealing the control bandwidth characteristics. The resulting Bode plots, shown in Fig. 7b, characterize the frequency response and control bandwidth for both actuators. The MAA achieves a bandwidth of 3.6 Hz at 20% stroke, decreasing to 1.6 Hz at 80% stroke. Similarly, the BAA exhibits a bandwidth of 2.2 Hz at 20% stroke, reducing to 0.6 Hz at 80% stroke. This reduction in bandwidth during larger displacements stems from two factors: the increased air volume required for greater motion ranges and the flow rate constraints imposed by both the FCVs' nominal diameter and the limited pressure differential available for actuation. However, the bandwidth could potentially be improved to 1~10 Hz through optimization of the pneumatic circuit and advanced control algorithms [46].

Fig. 7c shows the MAA tracking a 0.5 Hz sinusoidal trajectory at 50% stroke amplitude. The embedded sensor demonstrated excellent accuracy compared to ground truth measurements, achieving a MAE of 0.38 mm and RMSE of 0.46 mm. The overall control system maintained precise positioning with an MAE of 3.77 mm and RMSE of 4.22 mm. The duty cycle modulation of the inflating and deflating valves effectively maintained position control despite varying pressure differentials.

To assess dynamic performance and robustness, we conducted multi-step tracking and disturbance rejection tests, with results shown in Fig. 7d. The multi-step response exhibited an average settling time of 0.244 s with a steady-state error of 1.24 mm. In disturbance rejection tests, we manually applied random axial disturbances while maintaining a 60 mm target position. Over five trials, the system demonstrated robust recovery with an average settling time of 0.49 s and steady-state MAE of 1.06 mm, maintaining stability throughout all perturbations.

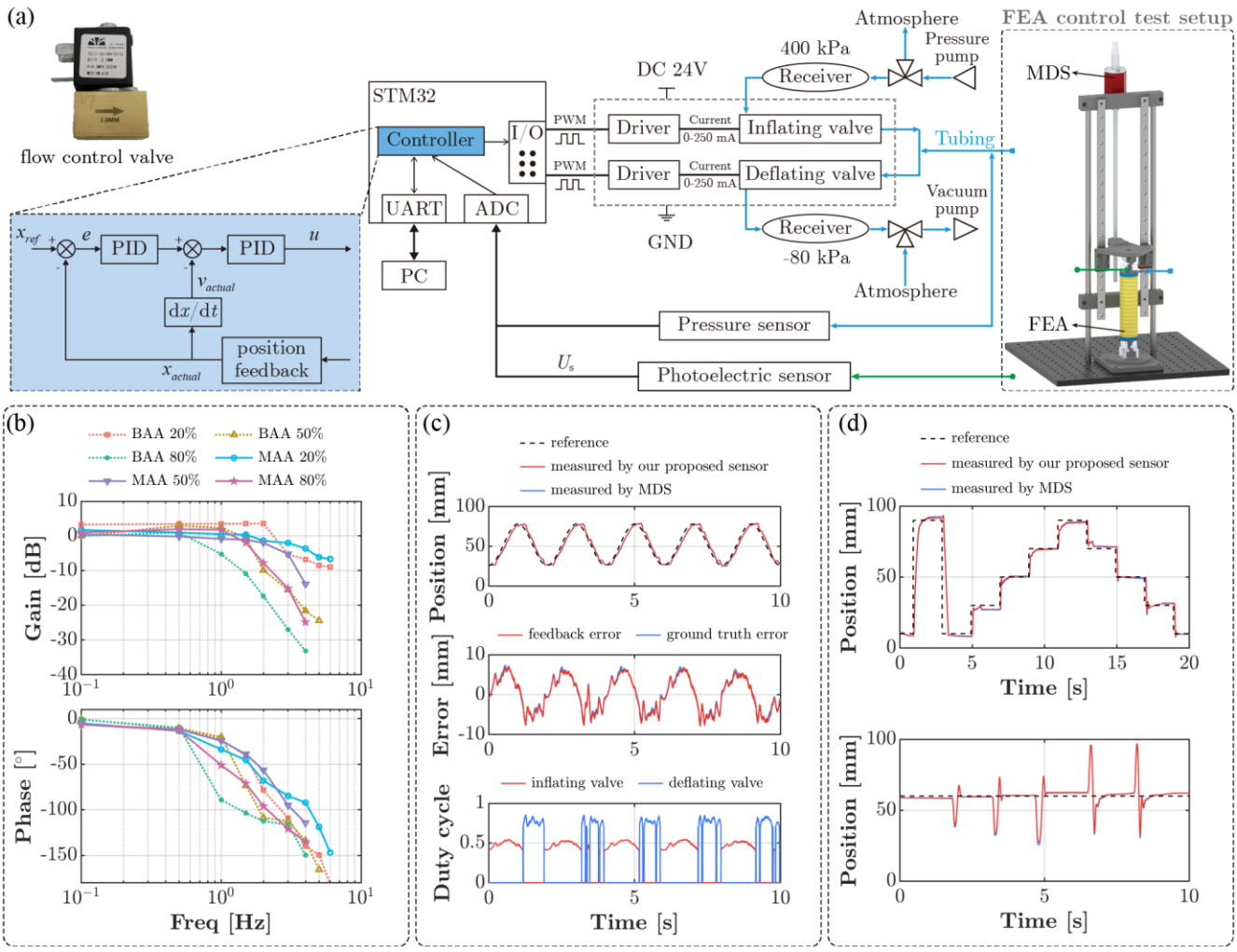

Fig. 7. Closed-loop control of FEAs. (a) The single-actuator control system architecture. (b) Bode diagram of the two actuators at different frequencies and amplitudes. (c) Sinusoidal displacement tracking results of the MAA. (d) Multi-step displacement tracking and disturbance rejection test results of the MAA.

IV. Bionic Leg Design

A. 2-DOF leg design

Drawing inspiration from musculoskeletal systems, we sought to implement two fundamental biological principles in our design: soft-rigid hybrid and joint coupling. Natural quadruped limbs demonstrate these principles effectively, with their back legs featuring three primary joints—hip, knee, and ankle—actuated by an intricate network of nine muscles (Fig. 8a). This architecture comprises three biarticular muscles (red lines) that span two joints and six monoarticular muscles (green lines) that act on single joints [47].

Previous researchers have made significant advances in bionic leg design, though they have often needed to address a fundamental constraint: because biological muscles and their artificial counterparts like McKibben muscles can only generate pulling forces, they require antagonistic pairs to achieve bidirectional motion [48]. This has led to well-established designs, such as two-links-with-six-muscles model (Fig. 8a-i) [49, 50]. We propose a potentially simpler approach through the use of FEAs capable of both extension and contraction, which may reduce the need for antagonistic arrangements. This approach allowed us to attempt a simplified architecture using just two actuators (MAA and BAA) as illustrated in Fig. 8a-ii and detailed in Fig. 8b.

In implementing this design, we aimed to optimize the spatial arrangement of components. We positioned the MAA and BAA on opposite sides of the leg's linkages, mounting them through bearings to help minimize mechanical interference (Fig. 8b). The MAA connects the hip and upper link for hip joint control, while the BAA connects the hip and lower link to enable coupled motion of both hip and knee joints. The leg structure was 3D printed in lightweight nylon with integrated channels for cables and air tubes (Fig. 8c). Our prototype achieves a range of motion of 120 degrees at both joints (Fig. 8d), while maintaining a relatively modest mass of

approximately 1 kg, with the FEAs accounting for half of this weight (Table I).

TABLE I. SPECIFICATIONS OF THE BIONIC LEG

Parameter	Range of motion/length	Mass (g)	Material
MAA	158 ~ 262 mm	196.3	VytaFlex60, carbon fiber tubes, and nylon
BAA	229 ~ 388 mm	294.4	
Hip	-60°~ 60°	155	nylon
Knee	0° ~ 120°	~	~
Upper leg	250 mm	86	nylon
Lower leg	250 mm	103.3	nylon
Others	~	164.6	~
Total mass	~	999.6	~

B. Leg kinematics

The kinematics of our 2-DOF bionic leg establishes the fundamental relationship between actuator lengths and foot position. Using a coordinate system fixed to the hip joint as shown in Fig. 8e, we can express the foot-end position (x, z) through the following equations:

$$\begin{bmatrix} x \\ z \end{bmatrix} = \begin{bmatrix} a_1 \sin\theta_1 + a_2 \sin(\theta_1 + \theta_2) \\ -a_1 \cos\theta_1 - a_2 \cos(\theta_1 + \theta_2) \end{bmatrix}, \quad (20)$$

where

$$\theta_1 = -90° + \arccos\frac{b_1^2 + d_1^2 - L_{MAA}^2}{2b_1 d_1} + \operatorname{artan}(\frac{1}{7}), \quad (21a)$$

$$\theta_2 = 150° - \arccos\frac{a_1^2 + e^2 - d_1^2}{2a_1 e} - \arccos\frac{b_2^2 + e^2 - L_{BAA}^2}{2b_2 e}, \quad (21b)$$

$$e = \sqrt{a_1^2 + d_2^2 - 2a_1 d_2 \cos(90° - \theta_1)}. \quad (21c)$$

The inverse kinematics can be expressed as follows:

$$\begin{bmatrix} \theta_1 \\ \theta_2 \end{bmatrix} = \begin{bmatrix} 90° - \operatorname{acos}\frac{a_1^2 + x^2 + z^2 - a_2^2}{2a_1\sqrt{x^2 + z^2}} - \operatorname{acos}\frac{x}{\sqrt{x^2 + z^2}} \\ \operatorname{acos}\frac{x^2 + z^2 - a_1^2 - a_2^2}{2a_1 a_2} \end{bmatrix}, \quad (22)$$

and

$$L_{MAA} = \sqrt{b_1^2 + d_1^2 - 2b_1 d_1 \cos(90° + \theta_1 - \beta_1)}, \quad (23a)$$

$$L_{BAA} = \sqrt{e^2 + b_2^2 - 2eb_2 \cos(180° - \theta_2 - \beta_2 - \operatorname{acos}\frac{e^2 + a_1^2 - d_2^2}{2ea_1})}. \quad (23b)$$

Through the inverse kinematics, we can map desired foot-end positions to the required FEA lengths, thus achieving controlled movement throughout the workspace. To establish the actuators' required displacement ranges during optimization, we analyzed four characteristic poses (Fig. 8f). Poses 1 and 4 define the vertical stride limits, while poses 2 and 3 determine both the horizontal stride length and the actuators' motion ranges. The relationship between joint angles and actuator lengths is shown in Fig. 8g, where the MAA length depends solely on θ_1, while the BAA length is a function of both θ_1 and θ_2.

To characterize the leg's theoretical workspace, randomly generating a comprehensive set of random joint angle combinations within the feasible range and computing the corresponding foot-end positions through forward kinematics. The resulting workspace boundary is illustrated in Fig. 8g.

C. Leg statics

The leg mechanism can be analyzed as a planar five-bar linkage system, treating the FEAs as rigid links connected to a fixed base (Fig. 8e). Through matrix-based static analysis of force equilibrium across the mechanism, we established the relationship between the FEAs' blocked forces and ground reaction force (GRF) throughout the workspace. Unlike conventional motor-driven legs that generate torques at joints, our design produces linear actuation forces directly through the MAA and BAA.

To simplify the static analysis, we made two key assumptions. First, while the mechanism uses revolute joints at points A, B, C, E, and F, we considered only their reaction forces, neglecting joint moments. Second, we modeled the foot-ground interaction as a single non-slip contact point, where the GRF comprises normal and friction components. This allowed us to treat the GRF at point D as a pure equilibrant force without an associated moment.

The force equilibrium conditions for the four moving links yield a system of linear equations, expressed in matrix form as:

$$\boldsymbol{C}\boldsymbol{F}_\mathbf{r} = \boldsymbol{D}\boldsymbol{F} \quad (24)$$

In Eq. (24), $\boldsymbol{F}_\mathbf{r}$ is the internal force vector containing the joint reaction components (F_{R15x}, F_{R15z}, F_{R12x}, F_{R12z}, F_{R23x}, F_{R23z}, F_{R25x}, F_{R25z}, F_{R34x}, F_{R34z}, F_{R45x}, F_{R45z}), and $\boldsymbol{F}$ is the external force vector containing the applied loads and actuator forces (M_1, F_{1x}, F_{1z}, M_2, F_{2x}, F_{2z}, M_3, F_{3x}, F_{3z}, M_4, F_{4x}, F_{4z}.). The 12×12 matrices $\boldsymbol{C}$ and $\boldsymbol{D}$ define the coefficient relationships for internal and external forces, respectively.

Using our statics model, we analyzed the required blocked forces for both actuators under various loads and poses. For a representative case—a single-leg squat supporting a 3 kg vertical load—we calculated the MAA and BAA forces across different configurations, assuming purely vertical loading without friction or acceleration effects (Fig. 8i). Our analysis indicated that a 100 N blocked force capacity in the non-compressed state would sufficiently support this motion. Based on the force-length characteristics shown in Fig. 4c, where blocked force minimizes at the maximum extension, we established the blocked force F_b to reach 100 N at maximum stroke as a key design parameter for both actuators.

D. Contact state detection

A key challenge in legged locomotion is detecting ground contact states while keeping the system as simple as possible. Rather than incorporating dedicated foot-mounted force sensors, we developed an alternative method to estimate contact states by analyzing the actuators' response to ground interaction. This approach examines how disturbance forces (ΔF_f) at the foot contact point (D) influence the blocked force (ΔF_b) of each actuator, which can be quantified using a sensitivity metric S:

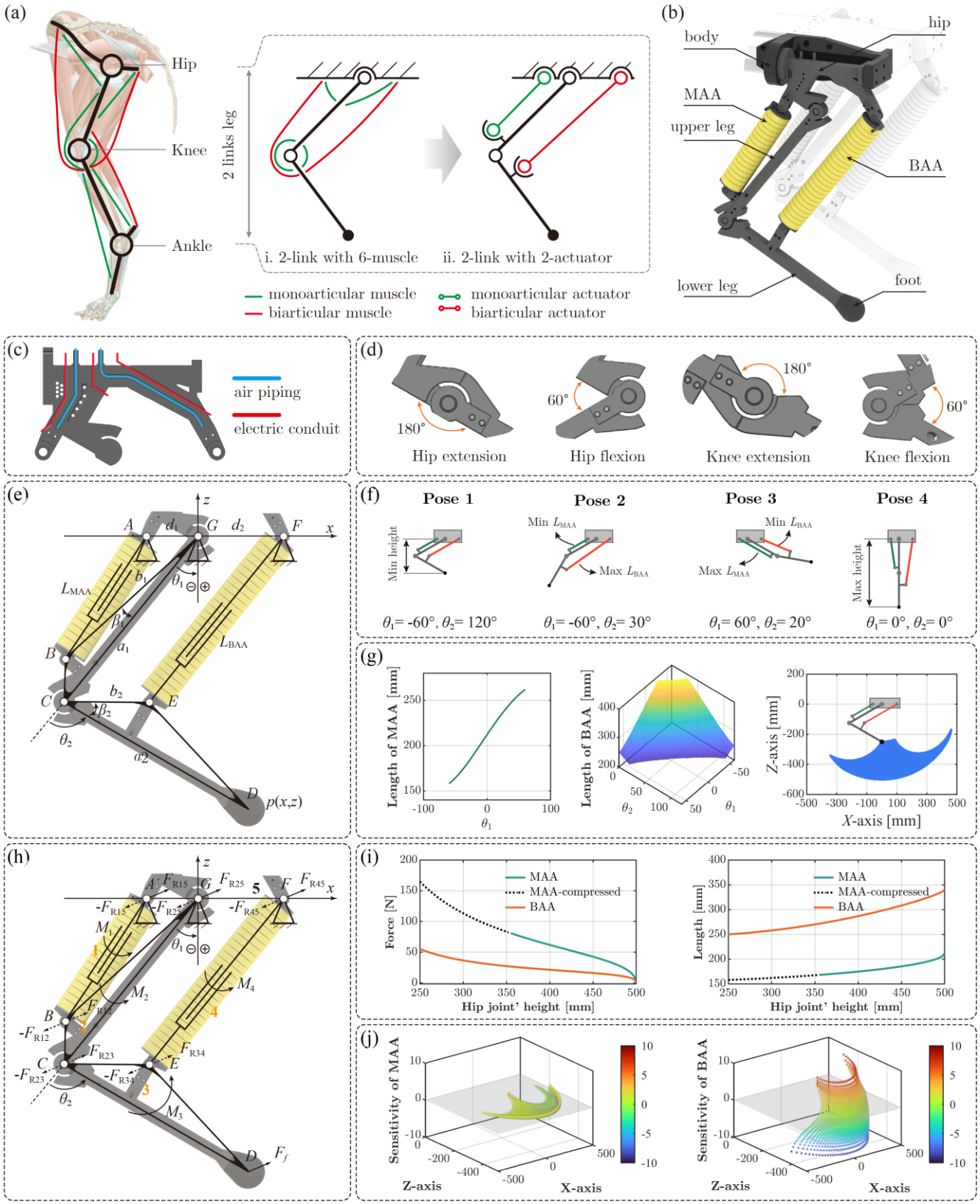

Fig. 8. Design, modeling and analysis of proposed bionic leg. (a) Diagrams of a natural hind leg and our designed leg. (b) Assembly view of the dual-actuator leg mechanism. (c) Structure of the hip joint with internally designed channels. (d) Range of motion for hip and knee joints. (e) Kinematic model and parameter definition. (f) Workspace analysis with extreme positions. (g) Actuator length relationships and theoretical workspace. (h) Static force analysis of the leg mechanism. (i) Theoretical force and length characteristics of FEAs at different heights. (j) Theoretical sensitivity analysis of FEAs' blocked force to GRF.

$$S=\frac{\Delta F_b}{\Delta F_f}. \quad (25)$$

The sensitivity analysis (Fig. 8j) revealed distinct response patterns for each actuator. A positive S indicates a tendency for the actuator to be compressed, while a negative S indicates a tendency to be stretched. At an operational height of 450 mm, the "touchdown" position (150 mm, -450 mm) showed that the BAA had significantly higher sensitivity ($S_{b,BAA}$ = 0.86) compared to the MAA ($S_{b,MAA}$ = -0.11). These distinct responses led us to select the changes in blocked force of the BAA as the primary metric for contact detection.

For practical implementation, we estimated the actuators' blocked forces using their known pressure-force relationship (Fig. 4c), along with existing displacement sensors and in-line pressure sensors. A threshold value for the blocked force change of the BAA was predefined, serving as an indicator for when the leg "touchdown". This threshold was determined experimentally, and the change in blocked force can be expressed as follows:

$$\Delta F_b=A_e\Delta P-k_s\Delta L. \quad (26)$$

In Eq. (26), A_e is the effective cross-sectional area, ΔP is the internal pressure change, ΔL is the displacement change, and k_s is the actuator stiffness. We neglected the friction of the telescopic sleeve, as its impact is minimal compared to other forces within the system. Thus, we believe it does not significant affect the conclusions drawn from our experimental setup. In such a manner, we were able to achieve the contact state detection without adding extra force sensors.

V. Bionic Leg Experiments

A. Leg workspace

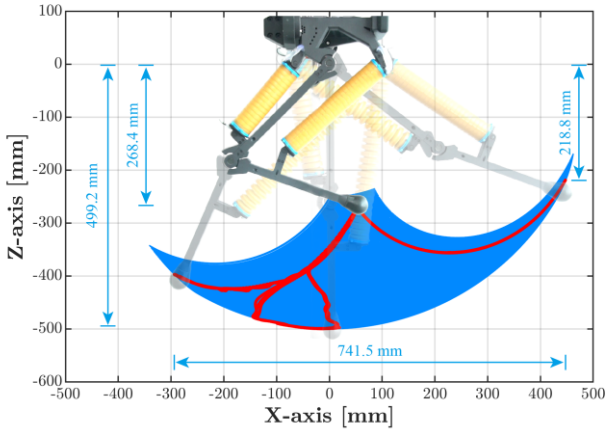

Fig. 9. Leg workspace. The red line illustrates the trajectory captured by the optoelectronic sensing system during testing, while the accompanying images show the four extreme positions.

To characterize the functional workspace of the bionic leg, we controlled the leg to reach its four extreme positions. The leg was rigidly mounted while the foot-end was positioned at the following extreme points: the most forward position, the most backward position, the highest position, and the lowest position (as demonstrated in the Supplementary Video). The foot-end trajectory was recorded using the embedded optoelectronic sensing system and plotted in Fig. 9, with snapshots of the leg at each extreme position.

The results indicate that the actual workspace of the leg closely resembles the theoretical workspace, which spans 741.5 mm along the X-axis and 280.4 mm along the Z-axis. However, the actual workspace was found to be slightly smaller than the theoretical workspace primarily due to the FEAs failing to achieve full compression, which could not be attained without applying sufficient external compressive load.

B. Leg squatting

We evaluated our FEAs' load-bearing capacity through squat tests (Fig. 10a). The bionic leg was mounted on a vertical linear guide with a 0.4 kg slider, constraining movement to the vertical direction. An OptiTrack V120 Trio motion capture system (NaturalPoint, Inc.) provided ground truth data, while a force/torque sensor measured GRF. The ground is a 3D-printed (PLA Basic, Bambu Lab) square plate with a small spherical indentation at its center, designed to interface with the foot-end and help keep the foot as close as possible directly beneath the hip joint. In the leg squatting and jumping experiments, the foot-end was also 3D printed using PLA to better interface with the ground.

During leg squatting, the leg followed a periodic vertical trajectory at 0.25 Hz, with the foot-end traversing between 350 - 450 mm. The embedded optoelectronic sensing system provided real-time feedback on the leg's position, which was cross-verified using data from the motion capture system. To test the system's robustness, squats were performed with external loads of 0.4 kg, 1.45 kg, and 2.45 kg. Fig. 10b shows the foot-end trajectory under 0.4 kg load, while Fig. 10c displays FEAs' displacement, tracking error, pressure, hip joint height, and GRF over time. Experimental data with other loads are presented in the supplementary video. We manually tuned the cascaded PID controller, omitting the integral term to prevent oscillations from cumulative tracking errors.

Under 0.4 kg load, the MAE for MAA and BAA position tracking were 2.4 mm and 4.5 mm respectively, with maximum absolute errors of 6.3 mm and 8.8 mm. The embedded sensor height tracking showed an MAE of 12.6 mm (~12.6% of the task scope). FEA pressures remained below operational limits, indicating potential for handling heavier loads. Maximum vertical forces increased from 15.2 N at 0.4 kg load to 27.7 N at 1.45 kg and 38.7 N at 2.45 kg, demonstrating the leg's ability to lift 2.45 times its own weight.

We observed non-uniform extension of the BAA due to bellows buckling under higher payloads. This behavior was anticipated given the inherent low axial stiffness of elastic bellows, and we have implemented several strategies to mitigate it. Specifically, we integrated a rigid telescopic sleeve, employed high-strength VytaFlex60 material, and optimized key structural parameters. While the complete elimination of buckling remains challenging, we consider its impact on the overall system performance to be acceptable. These results validate both the FEAs' load-bearing capacity and the effectiveness of their embedded sensing for closed-loop control.

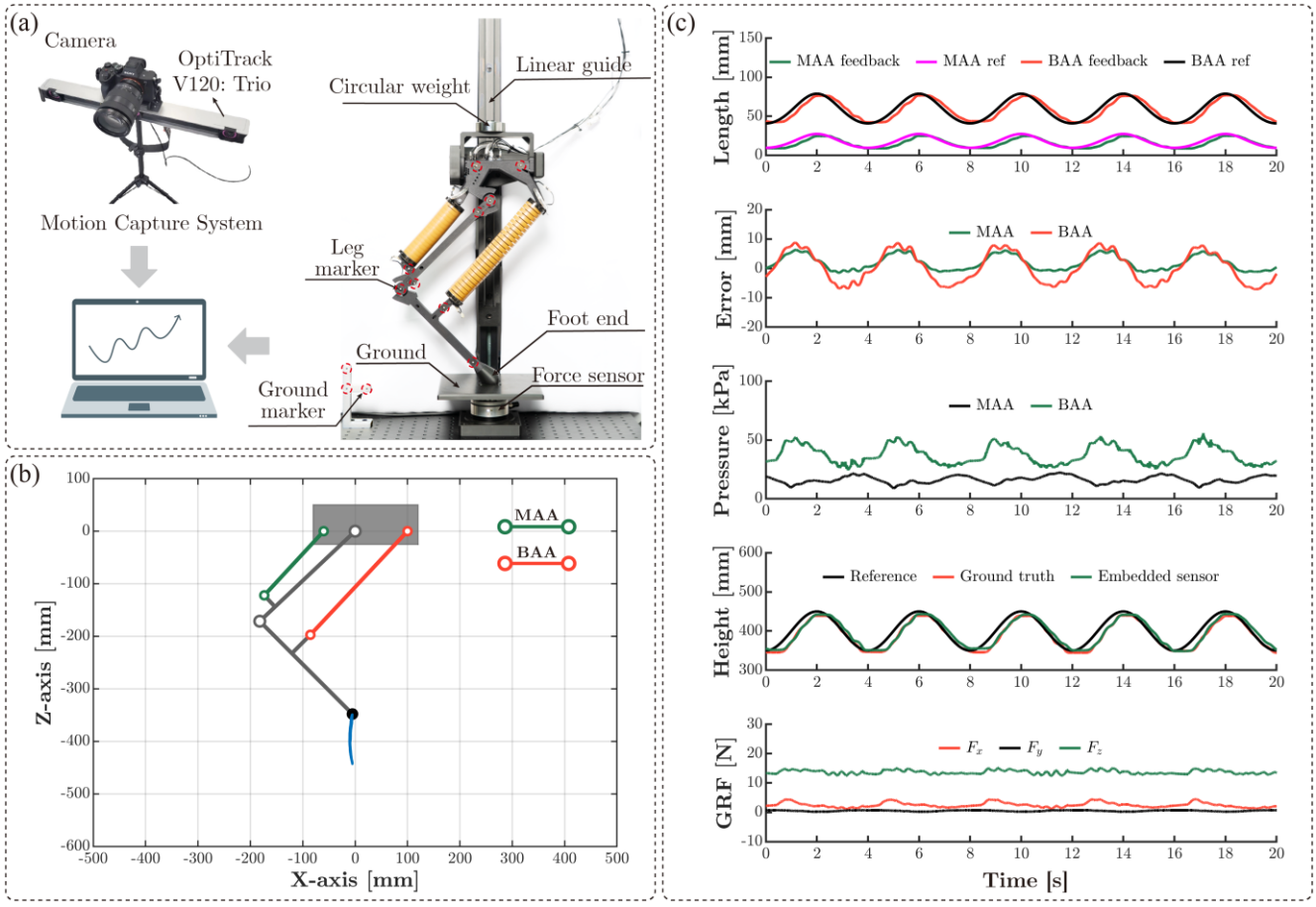

Fig. 10. Leg squatting. (a) Motion capture and experimental platform setup. (b) Leg trajectory during squatting motion under 0.4kg load. (c) Time-series measurements during squatting under 0.4kg load: actuator length, force, pressure, height and ground reaction force.

C. *Leg jumping*

To demonstrate the leg's dynamic capabilities, we conducted vertical jumping experiments using synchronized control of both actuators. The control strategy applied simultaneous 200ms high-pressure pulses to the MAA and BAA through their inflating FCVs, followed by deflation until pressure dropped below 0 kPa.

Fig. 11a shows the leg's motion sequence during a vertical jump (see supplementary video). Starting from the initial stance (MAA: -1.5kPa, BAA: -3kPa, hip height: 252mm), the leg progressed through push-off, flight, and landing phases within one second. Fig. 11a also presents the vertical displacement of the hip joint and foot-end during the jump. The hip joint reached a maximum height of 621mm at around 0.45s, while the foot-end peaked at 147mm at around 0.42s.

Fig. 11b shows the pressure responses of both actuators, which exhibited synchronized behavior but differed in amplitude due to their varying cavity volumes. The MAA peaked at 225 kPa and the BAA at 182 kPa during inflation, followed by controlled deflation through the FCVs. The system exhibits a latency of approximately 60-70ms between control signal transmission and actuator pressurization, primarily due to FCVs' mechanical response time and pneumatic line propagation delays. Pressure reduction demonstrates a shorter latency of approximately 10ms.

Fig. 11c depicts the GRF in the x and z directions during push-off and landing. The vertical forces (F_z) reached 36.5 N and 19.8 N, while horizontal forces (F_x) peaked at 10.5 N and 22.2 N. Notably, the hip joint's height remained continuous at ground contact, without sudden discontinuities. Upon landing, the foot height quickly reduced to zero while the hip joint height decreased gradually. Simultaneously, the vertical ground reaction force (F_z) emerged and increased steadily, indicating effective ground support by the single leg. The inherent compliance of the actuators played a crucial role in absorbing landing impacts, preventing bounce-back and demonstrating resilience to hard impacts.

D. *Leg walking*

We designed a simple gait for the hybrid leg's locomotion. The gait cycle comprises five distinct phases (Fig. 12a): (i) hip extension, (ii) hip extension, (iii) stance, (iv) hip flexion, and (v) knee flexion. Among these phases, the stance phase operates under position control, while the other four phases function in pressure control.

In our control framework, each FEA operates in one of three states: extending (positive pressure input causing axial elongation), contracting (negative pressure input leading to length reduction), or holding (two FCVs close, no air flow). During hip extension, the MAA extends to its desired position, while the BAA maintains its holding state. In the knee

extension phase, the BAA extends while the MAA holds. When the blocked force increment of BAA greater than 5 N, the BAA stops extending and enter the next phase. The stance phase then implements position control for both actuators, guiding the foot-end along a horizontal trajectory for a predetermined duration. Subsequently, during hip flexion, the MAA contracts to negative pressure while the BAA holds. The cycle ends with knee flexion, where the BAA contracts to negative pressure as the MAA maintains its holding state.

For experimental validation, we mounted the leg on a horizontal rail, maintaining a constant hip joint height of 450 mm above the ground. Fig. 12b shows the trajectory of the foot-end in Cartesian coordinates, while Fig. 12c gives the FEAs' displacement, tracking error during the "stance" phase, and the measured blocked force change of BAA over two walking cycles. During the stance phase, the maximum absolute tracking error of the FEAs remains under 10 mm. The BAA's blocked force change clearly indicated the ground contact events. As evidenced in the supplementary video, the single leg achieved stable walking at a velocity of 5.76 m/min. These results validate not only the effectiveness of our actuator design but also the integrated sensing and control strategy, while demonstrating the bionic leg's fundamental locomotion capabilities.

VI. Discussion

Skeletal muscle is commonly used as a benchmark in the field of bio-inspired robotics. Therefore, we begin by comparing the mechanical properties of FEAs with those of skeletal muscle, as presented in Table II. To provide a more comprehensive analysis, we then extend the comparison to include several widely used actuators, such as McKibben muscle (DMSP-40-200N-RM-RM, Festo), pneumatic cylinder (MAL 40X100-CA, AirTAC), hydraulic cylinder (ISA v5, Moog), and electro-mechanical actuator (EMA, Hu-MLS80S70-6R000, Zhejiang Hechuan Technology Co., Ltd.). In addition to our proposed FEAs, data for the other actuators are sourced from references [29, 45, 51-53], datasheets, and performance estimates based on their rated or maximum operating conditions. The superscripts "ex" and "co" denote the "extend" and "contract" states of the bidirectional fluid-driven actuators, respectively. This comparison evaluates key metrics, including maximum stroke, maximum strain

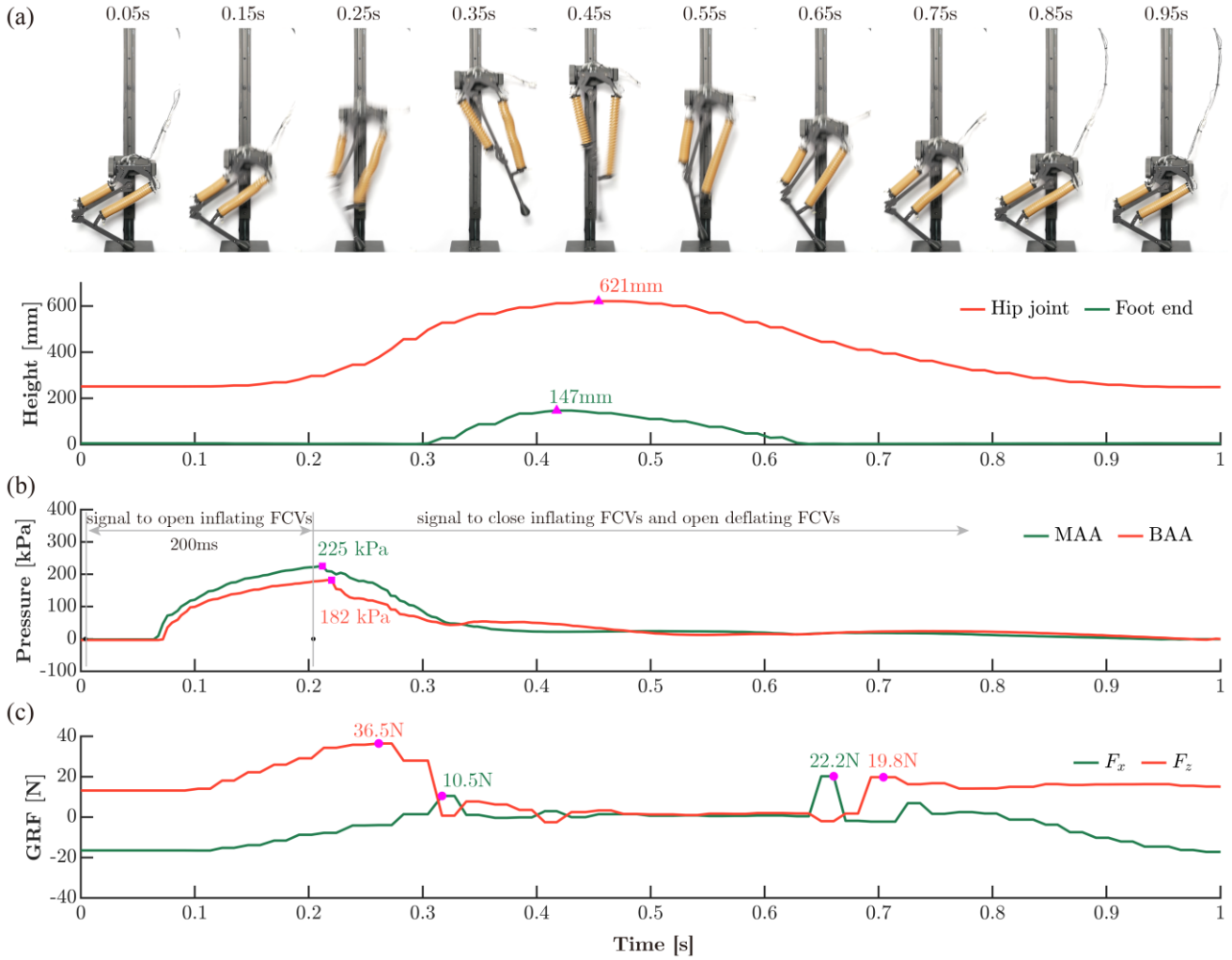

Fig. 11. Leg jumping. (a) Sequence of images showing the robotic leg during the vertical jump at different time intervals, along with the ground clearance heights of the hip joint and foot-end. (b) Pressure response and control signal of the MAA and BBA, showing the pressure buildup and release during the jumping motion. (c) GRF in the x and z directions, highlighting the leg's interaction with the ground during the push-off and landing phases.

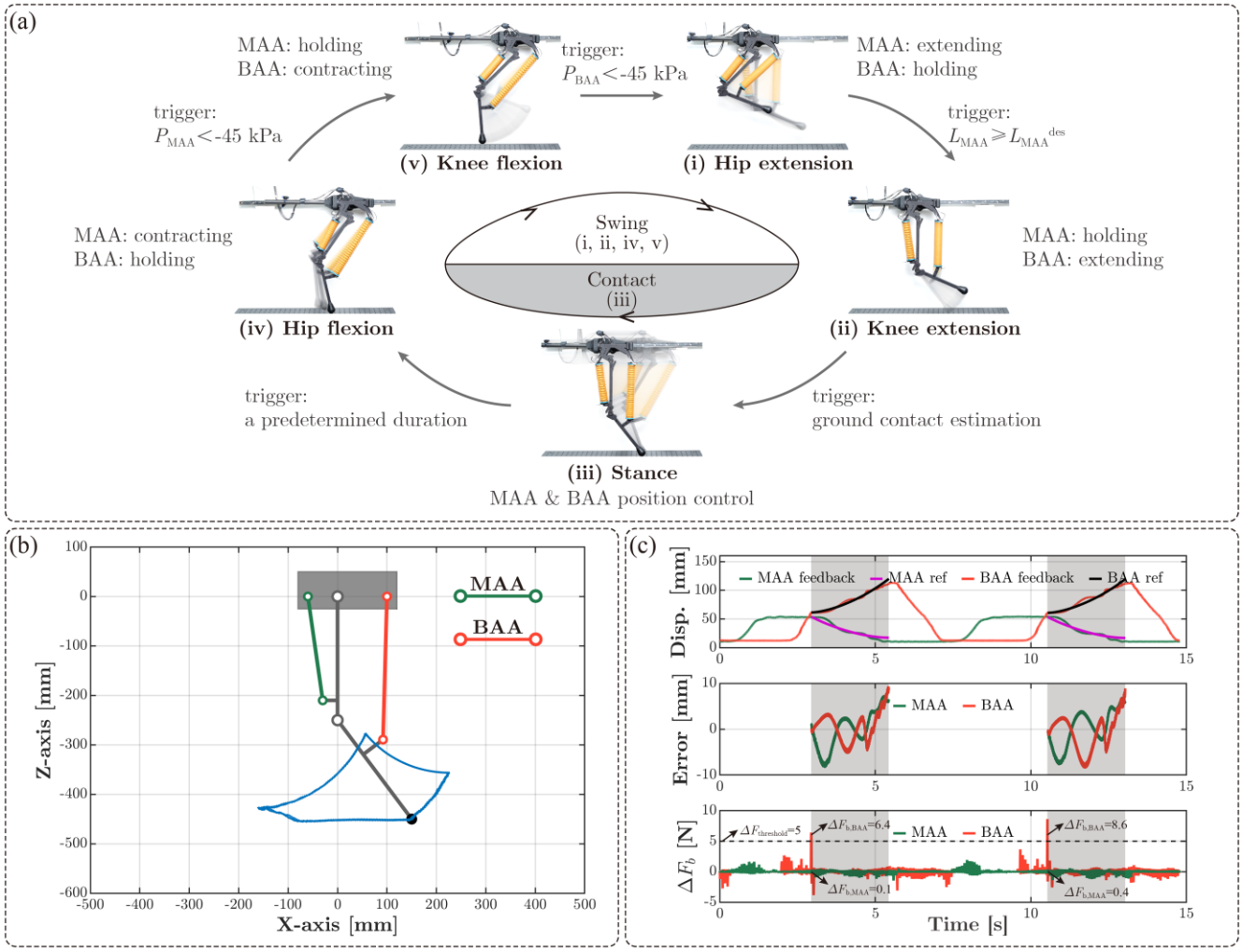

Fig. 12. Leg walking. (a) The walking gait composed of five phases. (b) The trajectory of the foot-end in Cartesian coordinates. (c) FEAs' displacement, tracking error, and blocked force change over two cycles of walking. The gray area represents the stance phase of the hybrid leg.

(relative to their closed pin-to-pin length), strain rate (achieves full stroke at maximum rated load), stress, modulus, energy densities, and power densities.

Our FEAs demonstrate remarkable strain capabilities (61% for MAA and 65% for BAA) that substantially exceed both skeletal muscles (20 - 40%) and commercial actuators, while maintaining bidirectional motion capability. This represents a substantial advancement in motion range, though the performance shows asymmetry between extension and contraction modes. The dynamic characteristics reveal promising velocities, with strain rates during extension (570 % s^{-1}) substantially surpassing skeletal muscle's typical range (10 - 50 % s^{-1}), even under conservative operating parameters (400 kPa positive pressure, -98 kPa negative pressure, and 2 mm orifice diameter). The asymmetry between extension (570% s^{-1}) and contraction rates (50% s^{-1} and 40% s^{-1}) can be attributed to the single-chamber design of our FEAs. While positive pressure actively drives extension through bellows inflation, contraction relies on the passive elastic restoration force of the actuator material, combined with negative pressure. This design choice simplifies the actuator structure but results in inherently different dynamics between the two motion phases.

The mechanical properties position FEAs in a distinctive intermediate space between biological and commercial actuators. Our FEAs' stress range (-0.07 to 0.14 MPa) is similar to that of skeletal muscle (0.1 to 0.35 MPa), indicating similar force generation capabilities. With densities of 980 - 990 kg/m³, our FEAs achieve material efficiency similar to skeletal muscle (1037 kg/m³) and pneumatic actuators, while offering significant weight advantages over traditional hydraulic actuator (~2100 kg/m³) and EMA (~6700 kg/m³). The modulus of our FEAs (2.07 MPa) places them between skeletal muscle (0.02-0.1 MPa) and McKibben muscles (~47 MPa), reflecting an intentional design choice favoring compliance over pure force output. This aligns with known limitations of pneumatic systems, which typically operate at lower pressures (around 600 kPa) compared to hydraulic systems (21 MPa) due to safety considerations and material constraints.

The energy and power density analysis reveals interesting scale-dependent behavior of our FEAs. In terms of volumetric energy density, while our FEAs demonstrate biological parity, they fall short of commercial actuators. Similarly, their mass-specific energy density exceeds that of skeletal muscle but remains lower than McKibben muscle (~230 J kg^{-1}) and pneumatic cylinder (~150 J kg^{-1}), reflecting the inherent energy

storage limitations of our lower operating pressure. When examining power density, a different pattern emerges. While the volumetric power density of our FEAs is lower than commercial alternatives like EMA and pneumatic actuators, their mass-specific power density shows more competitive performance. They outperform both skeletal muscle (48-274 W kg^{-1}) and EMA (100-350 W kg^{-1}), though still falling short of pneumatic cylinders (~1360 W kg^{-1}) and hydraulic actuator (~2800 W kg^{-1}).

Although both metrics fall short of hydraulic actuator, this performance profile suggests FEAs are particularly advantageous in applications requiring high-power, high-strain operations where weight minimization is critical. The current performance gap relative to commercial pneumatic actuators can be partly attributed to our conservative operating parameters, suggesting potential for improvement through higher air flow and operating pressure, while still maintaining the inherent safety and compliance benefits of pneumatic operation. However, this limitation also highlights a fundamental challenge in pneumatic systems, where the need for safety and compliance often requires operating at lower pressures, which can limit the high specific power that might otherwise be achievable.

The fundamental design of our FEAs highlights an inherent trade-off between compliance and output force, similar to what has been observed in other soft pneumatic actuators (SPAs) [54]. This trade-off is particularly evident in the relationship between operating pressure and material selection: while higher pressures can increase force output, they require stiffer materials, which compromise the desired compliance. However, the elastic bellows and telescopic sleeve in our FEAs have shown promise in balancing this trade-off, offering high stroke ratios while enhancing pressure handling capabilities. Several promising optimization pathways could further improve the performance of our proposed FEAs. These include the use of high-modulus, low-hysteresis silicone rubbers (such as Smooth-Sil 950/960), the implementation of advanced mechanical designs incorporating fiber reinforcement and reinforcement rings, and operation at higher pressure differentials through larger-orifice FCVs.

TABLE II. COMPARISON OF OUR ACTUATORS, SKELETAL MUSCLE, AND COMMERCIAL ACTUATORS.

		MAA	**BAA**	**Skeletal muscle**	**McKibben Muscle**	**Pneumatic Cylinder**	**Hydraulic actuator**	**EMA**
Operating conditions		Inflation: 400 kPa Deflation: -98 kPa Orifice Diameter: 2 mm		——	Inflation: 1 MPa Orifice Diameter: 2 mm		Inflation: 21 MPa Max. flow: 13 L/min	48 VDC
Direction		Bi-dir.	Bi-dir.	Uni-dir.	Uni-dir.	Bi-dir.	Bi-dir.	Bi-dir.
Max. stroke [mm]		~ 104	~ 159	——	~ 60	100	100	70
Max. strain [%]		~ 61	~ 65	20 – 40	~ 17	~ 24	~ 33	~ 27
Strain rate [% s^{-1}]		570^{ex} 50^{co}	570^{ex} 40^{co}	10 – 50	~ 50	10 – 300	~ 90	30 – 42
Stress [MPa]		-0.07 – 0.13	-0.06 – 0.14	0.1 – 0.35	< 2.4	0.1 – 1.0	~ 21	~ 2.8
Density [kg m^{-3}]		~ 980	~ 990	1037	~ 850	~ 780	~ 2100	~ 6700
Modulus [MPa]		2.07		0.02 – 0.1	~ 47	> 1000		
Energy density	[kJ m^{-3}]	~ 86	~ 95	8 – 40	~ 190	~ 110	~ 990	620 – 1500
	[J kg^{-1}]	~ 88	~ 96	8 – 39	~ 230	~ 150	~ 470	90 – 224
Power density	[kW m^{-3}]	~ 740^{ex} ~ 66^{co}	~ 780^{ex} ~ 55^{co}	50 – 248	~ 560	~ 1050	~ 5900	710 – 2400
	[W kg^{-1}]	~ 760^{ex} ~ 67^{co}	~ 790^{ex} ~ 55^{co}	48 – 274	~ 660	~ 1360	~ 2800	100 – 350

In pursuing biomimetic principles while minimizing system complexity, we prioritized a design with minimal joints and actuators. Although our two-FEA configuration reduces complexity, it sacrifices two key features of biological musculoskeletal systems: stiffness adjustment and mechanical redundancy. Unlike skeletal muscles that operate through active contraction, our FEAs enable bidirectional motion. This configuration's primary limitation lies in restricted stiffness modulation, which depends primarily on the FEAs' material properties and pressure. The design also lacks the fault tolerance seen in biological systems, due to the absence of redundant actuators. While this simplification allowed us to focus on fundamental biomimetic principles, it may not match the practicality of electrically-driven legged robots. Future improvements could incorporate variable stiffness actuators to enhance system adaptability and explore novel architectural designs, such as bending or rotary actuators at the joints [55], to create an antagonistic mechanism with the linear FEAs.

Our implementation of an active control musculoskeletal leg with embedded sensing demonstrates sufficient feedback control bandwidth for maintaining stability and performance in low-speed tasks, as evidenced by squatting and walking experiments. The soft FEAs in our hybrid system reduce overall stiffness, achieving more naturalistic actuation, but this comes at the cost of limited bandwidth, nonlinearity, and increased control complexity. Simply tuning PID controller

gains for faster response tends to induce instability or oscillation. The current performance, with maximum absolute tracking errors of approximately 10 mm, represents a balance between control accuracy and stability. Future work could explore advanced approaches such as Model Predictive Control (MPC), adaptive control, and learning-based methods. Notably, consistent with existing research in soft robotics [56] and compliant systems [6], incorporating articulated soft structures and elastic components into robotic legs can reduce reliance on high-frequency, high-precision feedback control. To develop more advanced robotic systems, it is meaningful to explore strategies that balance these conflicting factors.

Although synchronized high-pressure pulse control of the MAA and BAA enabled stable vertical jumping, several aspects still require optimization to accommodate more dynamic scenarios. The passive nature of the foot-end trajectory and landing point during the flight phase suggests that there is room for improvement in both attitude and trajectory control. Additionally, the observed non-zero F_x in the initial state points to opportunities for better GRF management. Further investigation into the leg dynamics could help refine the actuation strategy, including pressure amplitude variation, pulse duration optimization and reduction of system delays. To execute more dynamic tasks, such as performing exotic motions or traversing unstructured terrain, both structural refinements and advanced dynamic control strategies will likely be necessary.

VII. Conclusion

In this paper, we presented and validated a musculoskeletal bionic leg actuated by FEAs, demonstrating the viability of artificial muscles in legged robotics. Through systematic optimization of the actuator structure, we achieved enhanced output force while integrating compact optoelectronic sensing for robust closed-loop control. The leg's performance was evaluated through a comprehensive suite of experiments, including load-bearing squats, dynamic jumping, and controlled walking gaits. Our results demonstrate that FEAs can achieve both the high energy density and substantial dynamic deformation necessary to effectively mimicking biological muscle function. The novel embedded optical sensing system not only reduced the overall system mass but also eliminated the complexity associated with conventional external force sensors.

While our results highlight the promise of FEAs, several technical challenges remain to be addressed. The inherent nonlinear behavior and relatively low mechanical stiffness of these actuators present ongoing challenges for precise motion control. Future work should focus on optimizing FEA material composition and structural design to enhance force output and dynamic response characteristics. Additionally, the development of more advanced control strategies could improve the adaptability of FEA-driven robots in unstructured environments.

In conclusion, this work demonstrates the promising potential of FEAs as artificial muscles in bio-inspired robotics. Our findings provide a solid foundation for the development of hybrid legged platforms capable of efficiently replicating the biological locomotion abilities observed in natural systems.

Appendix A

Algorithm 1 Enumeration-based optimization

Input: $L_{max}, L_{min}, R_{max}, F_b, E, \sigma_m, \mu$
Output: $n, a, b, c, d, e, h, V_0, P_b, F_{cr}, U$

Initialize
for each n **do**
  for each h **do**
    for each d **do**
      $L_c \leftarrow n(2h+d) - L_{\min}$
      $c \leftarrow \text{round}(nd/(n-1))$
      $L_0 \leftarrow n(2h+d) + c(n-1)$
      $w^t_{\max} \leftarrow (L_{\max} - L_0)/(2n)$
      if $(w^t_{\max} \le kh)$ and $(L_c \in$ buffer distance$)$ **then**
        $b \leftarrow R_{\min}$
        $D \leftarrow Eh^3/(12(1-\mu^2))$
        for each P_i **do**
          Compute e_i based on $\sigma_{eq} = \sigma_m/\eta$
          $a_i \leftarrow R_{\max} - e_i$
          Compute $w_{\max i}$ at $F = F_b, P = P_i$
        end for
        P_b that $2nw^t_{\max} = L_{\max} - L_0 \leftarrow$ interpolate $(w_{\max i}, P_i)$
        Compute e
        $a \leftarrow R_{\max} - e$
        $V_0 \leftarrow \pi b^2 n(2h+d) + \pi a^2(n-1)c$
        $L_0 \leftarrow n(2h+d) + c(n-1)$
        $\zeta \leftarrow b/a$
        $\varepsilon \leftarrow -(1+\zeta^2)(1-\zeta)^3/(3(1-\zeta^2+(1+\zeta^2)\ln\zeta))$
        $F_{cr} \leftarrow \pi^3 \varepsilon E h^3 a^3/(2nL_0(b-a)^3(1-\mu^2))$
        $P'_b \leftarrow mapminmax(P_b, 0, 1)$
        $V'_0 \leftarrow mapminmax(V_0, 0, 1)$
        $F'_{cr} \leftarrow mapminmax(F_{cr}, 1, 0)$
        $U \leftarrow \lambda_1 P'_b + \lambda_2 V'_0 + \lambda_3 F'_{cr}$
        Record $n, a, b, c, d, e, h, V_0, P_b, F_{cr}, U$
      end if
    end for
  end for
end for

References

[1] H. Taheri and N. Mozayani, "A study on quadruped mobile robots," *Mech. Mach. Theory,* vol. 190, 2023, Art no. 105448.

[2] D. Wooden, M. Malchano, K. Blankespoor, A. Howardy, A. A. Rizzi, and M. Raibert, "Autonomous navigation for BigDog," in *Proc. IEEE Int. Conf. Robot. Autom.*, 2010.

[3] P. M. Wensing, A. Wang, S. Seok, D. Otten, J. Lang, and S. Kim, "Proprioceptive actuator design in the mit cheetah: Impact mitigation and high-bandwidth physical interaction for dynamic legged robots," *IEEE Trans. Robot.,* vol. 33, no. 3, pp. 509-522, 2017.

[4] F. L. Moro *et al.*, "Horse-like walking, trotting, and galloping derived from kinematic Motion Primitives (kMPs) and their application to walk/trot transitions in a compliant quadruped robot," *Biol. Cybern.,* vol. 107, no. 3, pp. 309-320, 2013.

[5] R. Baines *et al.*, "Multi-environment robotic transitions through adaptive morphogenesis," *Nature,* vol. 610, no. 7931, pp. 283-289, 2022, doi: 10.1038/s41586-022-05188-w.

[6] L. Liow *et al.*, "A compliant robotic leg based on fibre jamming," *IEEE Trans. Robot.,* vol. 40, pp. 4578-4597, 2024.

[7] M. Ang, O. Khatib, and B. Siciliano, *Encyclopedia of Robotics*. Heidelberg: Springer, 2021, p. 4000.

[8] J. Zhang *et al.*, "Robotic artificial muscles: Current progress and future perspectives," *IEEE Trans. Robot.,* vol. 35, no. 3, pp. 761-781, 2019.

[9] K. Narioka, A. Rosendo, A. Sproewitz, and K. Hosoda, "Development of a minimalistic pneumatic quadruped robot for fast locomotion," in *Proc. IEEE Int. Conf. Robot. Biomimetics.*, 2012.

[10] S. Nakatsu, A. Rosendo, M. Shimizu, and K. Hosoda, "Realization of three-dimensional walking of a cheetah-modeled bio-inspired quadruped robot," in *Proc. IEEE Int. Conf. Robot. Biomimetics.*, 2014.

[11] H. Tanaka, T. Y. Chen, and K. Hosoda, "Dynamic turning of a soft quadruped robot by changing phase difference," *Front. Robot. AI,* vol. 8, 2021, Art no. 629523.

[12] K. S. Aschenbeck, N. I. Kern, R. J. Bachmann, and R. D. Quinn, "Design of a quadruped robot driven by air muscles," in *Proc. First IEEE/RAS-EMBS Int. Conf. Biomed. Robotics Biomech.*, 2006.

[13] X. Wang, M. Li, W. Guo, P. Wang, and L. Sun, "Development of an antagonistic bionic joint controller for a musculoskeletal quadruped," in *Proc. IEEE/RSJ Int. Conf. Intell. Robots Syst.*, 2013.

[14] Y. Yamada, S. Nishikawa, K. Shida, R. Niiyama, and Y. Kuniyoshi, "Neural-body coupling for emergent locomotion: A musculoskeletal quadruped robot with spinobulbar model," in *Proc. IEEE/RSJ Int. Conf. Intell. Robots Syst.*, 2011.

[15] R. F. Shepherd *et al.*, "Multigait soft robot," *Proc. Natl. Acad. Sci. U.S.A.,* vol. 108, no. 51, pp. 20400-20403, 2011.

[16] D. Drotman, S. Jadhav, D. J. Sharp, C. Chan, and M. T. Tolley, "Electronics-free pneumatic circuits for controlling soft-legged robots," *Sci. Robot.,* vol. 6, no. 51, 2021, Art no. eaay2627.

[17] S. Li *et al.*, "Scaling up soft robotics: A meter-scale, modular, and reconfigurable soft robotic system," *Soft Robot.,* vol. 9, no. 2, pp. 324-336, 2022.

[18] H. Zhao, Y. Li, A. Elsamadisi, and R. F. Shepherd, "Scalable manufacturing of high force wearable soft actuators," *Extreme Mech. Lett.,* vol. 3, pp. 89-104, 2015.

[19] H. K. Yap, H. Y. Ng, and C. H. Yeow, "High-force soft printable pneumatics for soft robotic applications," *Soft Robot.,* vol. 3, no. 3, pp. 144-158, 2016.

[20] K. Han, N.-H. Kim, and D. Shin, "A novel soft pneumatic artificial muscle with high-contraction ratio," *Soft Robot.,* vol. 5, no. 5, pp. 554-566, 2018.

[21] X. Dong, C. Tang, S. Jiang, Q. Shao, and H. Zhao, "Increasing the payload and terrain adaptivity of an untethered crawling robot via soft-rigid coupled linear actuators," *IEEE Robot. Autom. Lett.,* vol. 6, no. 2, pp. 2405-2412, 2021.

[22] J. Zhang *et al.*, "Geometric confined pneumatic soft–rigid hybrid actuators," *Soft Robot.,* vol. 7, no. 5, pp. 574-582, 2020.

[23] J. Zhu *et al.*, "Bioinspired Multimodal Multipose Hybrid Fingers for Wide-Range Force, Compliant, and Stable Grasping," *Soft Robot.,* vol. 10, no. 1, pp. 30-39, 2023.

[24] Y. Cui, X.-J. Liu, X. Dong, J. Zhou, and H. Zhao, "Enhancing the Universality of a Pneumatic Gripper via Continuously Adjustable Initial Grasp Postures," *IEEE Trans. Robot.,* vol. 37, no. 5, pp. 1604-1618, 2021.

[25] F. Chen and M. Y. Wang, "Design optimization of soft robots: A review of the state of the art," *IEEE Robot. Autom. Mag.,* vol. 27, no. 4, pp. 27-43, 2020.

[26] P. Moseley, J. M. Florez, H. A. Sonar, G. Agarwal, W. Curtin, and J. Paik, "Modeling, design, and development of soft pneumatic actuators with finite element method," *Adv. Eng. Mater.,* vol. 18, no. 6, pp. 978-988, 2016.

[27] C.-H. Liu, L.-J. Chen, J.-C. Chi, and J.-Y. Wu, "Topology optimization design and experiment of a soft pneumatic bending actuator for grasping applications," *IEEE Robot. Autom. Lett.,* vol. 7, no. 2, pp. 2086-2093, 2022.

[28] F. Chen, Z. Song, S. Chen, G. Gu, and X. Zhu, "Morphological Design for Pneumatic Soft Actuators and Robots With Desired Deformation Behavior," *IEEE Trans. Robot.,* vol. 39, no. 6, pp. 4408-4428, 2023.

[29] D. R. Higueras-Ruiz, K. Nishikawa, H. Feigenbaum, and M. Shafer, "What is an artificial muscle? A comparison of soft actuators to biological muscles," *Bioinspir. Biomim.,* vol. 17, no. 1, 2021, Art no. 011001.

[30] M. S. Xavier *et al.*, "Soft pneumatic actuators: A review of design, fabrication, modeling, sensing, control and applications," *IEEE Access,* vol. 10, pp. 59442-59485, 2022.

[31] L. O. Tiziani, T. W. Cahoon, and F. L. Hammond, "Sensorized pneumatic muscle for force and stiffness control," in *Proc. IEEE Int. Conf. Robot. Autom.*, 2017.

[32] B. Shih, J. Mayeda, Z. Huo, C. Christianson, and M. T. Tolley, "3D printed resistive soft sensors," in *Proc. IEEE Int. Conf. Soft Robot.*, 2018.

[33] O. Azami, D. Morisaki, T. Miyazaki, T. Kanno, and K. Kawashima, "Development of the extension type pneumatic soft actuator with built-in displacement sensor," *Sens. Actuators, A,* vol. 300, 2019, Art no. 111623.

[34] M. G. Antonelli, P. Beomonte Zobel, A. De Marcellis, and E. Palange, "Design and Characterization of a Mckibben Pneumatic Muscle Prototype with an Embedded Capacitive Length Transducer," *Machines,* vol. 10, no. 12, 2022, Art no. 1156.

[35] H. Zhao, K. O'Brien, S. Li, and R. F. Shepherd, "Optoelectronically innervated soft prosthetic hand via stretchable optical waveguides," *Sci. Robot.,* vol. 1, no. 1, 2016, Art no. eaai7529.

[36] L. O. Tiziani and F. L. Hammond, "Optical sensor-embedded pneumatic artificial muscle for position and force estimation," *Soft Robot.,* vol. 7, no. 4, pp. 462-477, 2020.

[37] J. Jung, M. Park, D. Kim, and Y.-L. Park, "Optically sensorized elastomer air chamber for proprioceptive sensing of soft pneumatic actuators," *IEEE Robot. Autom. Lett.,* vol. 5, no. 2, pp. 2333-2340, 2020.

[38] B. Jamil and Y. Choi, "Modified stiffness-based soft optical waveguide integrated pneumatic artificial muscle (PAM) actuators for contraction and force sensing," *IEEE/ASME Trans. Mechatron.,* vol. 26, no. 6, pp. 3243-3253, 2021.

[39] W. Fan, J. Wang, Z. Zhang, G. Chen, and H. Wang, "Vacuum-Driven Parallel Continuum Robots With Self-Sensing Origami Linkages," *IEEE/ASME Trans. Mechatron.,* vol. 39, no. 5, pp. 3370 - 3380, 2024.

[40] G. Zöller, V. Wall, and O. Brock, "Acoustic sensing for soft pneumatic actuators," in *Proc. IEEE/RSJ Int. Conf. Intell. Robots Syst.*, 2018.

[41] E. Ventsel and T. Krauthammer, *Thin Plates and Shells: Theory, Analysis, and Applications*. New York: Marcel Dekker, 2001, p. 688.

[42] A. Ü. Keskin, *Boundary Value Problems for Engineers with MATLAB Solutions*. Cham: Springer, 2019, p. 517.

[43] X. Dong, Y. Wang, X. J. Liu, and H. Zhao, "Development of modular multi-degree-of-freedom hybrid joints and robotic flexible legs via fluidic elastomer actuators," *Smart Mater. Struct.,* vol. 31, no. 3, 2022, Art no. 035034.

[44] W. C. Young, R. G. Budynas, and A. M. Sadegh, *Roark's Formulas for Stress and Strain*. New York: McGraw-Hill, 2002, p. 854.

[45] S. M. Mirvakili and I. W. Hunter, "Artificial muscles: Mechanisms, applications, and challenges," *Adv. Mater.,* vol. 30, no. 6, 2018, Art no. 1704407.

[46] Y. Wang, X.-J. Liu, and H. Zhao, "Speeding up soft pneumatic actuators through pressure and flow dynamics modeling and optimization," *Extreme Mech. Lett.,* vol. 57, p. 101914, 2022.

[47] P. E. Hudson, S. A. Corr, R. C. Payne-Davis, S. N. Clancy, E. Lane, and A. M. Wilson, "Functional anatomy of the cheetah (Acinonyx jubatus) hindlimb," *J. Anat.,* vol. 218, no. 4, pp. 363-374, 2011.

[48] J. Lei, J. Zhu, P. Xie, and M. Tokhi, "Joint variable stiffness of musculoskeletal leg mechanism for quadruped robot," *Adv. Mech. Eng.,* vol. 9, no. 4, 2017, Art no. 1687814017690342.

[49] A. H. Fagg, N. Sitkoff, A. G. Barto, and J. C. Houk, "Cerebellar learning for control of a two-link arm in muscle space," in *Proc. IEEE Int. Conf. Robot. Autom.*, 1997.

[50] H. Ochi, H. Kino, K. Tahara, and Y. Matsutani, "Geometric conditions of a two-link-and-six muscle structure based on internal force stability," *Robomech J.,* vol. 7, p. 16, 2020, Art no. 17.

[51] M. Li, A. Pal, A. Aghakhani, A. Pena-Francesch, and M. Sitti, "Soft actuators for real-world applications," *Nat. Rev. Mater.,* vol. 7, no. 3, pp. 235-249, 2022.

[52] J. E. Huber, N. A. Fleck, and M. F. Ashby, "The selection of mechanical actuators based on performance indices," *Proc. R. Soc. Lond. A.,* vol. 453, no. 1965, pp. 2185-2205, 1997.

[53] V. Barasuol *et al.*, "Highly-integrated hydraulic smart actuators and smart manifolds for high-bandwidth force control," *Front. Robot. AI,* vol. 5, 2018 2018, Art no. 51.

[54] A. Goswami and P. Vadakkepat, *Humanoid Robotics: A Reference*. Dordrecht: Springer, 2018, p. 2676.

[55] Z. Jiang, Y. Wang, and K. Zhang, "Development of a Pneumatically Actuated Quadruped Robot Using Soft–Rigid Hybrid Rotary Joints," *Robotics,* vol. 13, no. 2, p. 24, 2024.

[56] A. Albu-Schaffer *et al.*, "Soft robotics," *IEEE Robot. Autom. Mag.,* vol. 15, no. 3, 2008.